NACA0015 Measurements in LM Wind Tunnel and Turbulence Generated Noise

Bertagnolio, Franck

Publication date:
2008

Document Version
Publisher's PDF, also known as Version of record

Risø DTU
National Laboratory
for Sustainable Energy

DTU

Risø-R-Report

NACA0015 Measurements in LM Wind Tunnel and Turbulence Generated Noise

Franck Bertagnolio

Risø-R-1657(EN)

Risø National Laboratory for Sustainable Energy
Technical University of Denmark
Roskilde, Denmark
November 2008

DTU

Author: Franck Bertagnolio
Title: NACA0015 Measurements in LM Wind Tunnel and Turbulence Generated Noise
Division: Wind Energy Division

Risø-R-1657(EN)
November 2008

Abstract (max. 2000 char.):

A NACA0015 airfoil section was instrumented with an array of highfrequency microphones mounted on its surface and measured in the wind tunnel at LM Glasfiber at various inflow speeds, angles of attack, and with different turbulent inflow conditions. The aim of this work is to analyze these measurement data, including the turbulent inflow characteristics. The airfoil surface pressure data are considered in the perspective of turbulent inflow noise in order to identify the potential for using these data to validate and possibly improve associated noise models from the literature. In addition, these data are further analyzed in
the context of trailing edge noise modeling which is directly related to the surface pressure fluctuations in the vicinity of the trailing edge.

ISSN 0106-2840
ISBN 978-87-550-3701-4

Contract no.:
EFP-2008 / ENS-33033-0266

Group's own reg. no.:
1110044-00

Sponsorship:

Cover :

Pages: 63
Tables: 3
References: 27

Information Service Department
Risø National Laboratory for Sustainable Energy
Technical University of Denmark
P.O.Box 49
DK-4000 Roskilde
Denmark
Telephone +45 46774004
bibl@risoe.dk
Fax +45 46774013
www.risoe.dtu.dk

Contents

1 Introduction

The study conducted in this report is part of a longer project which aim is to gain a better understanding of various flow phenomena that occur in the flow field around wind turbine airfoils, such as boundary layer transition, separation, turbulent inflow noise, trailing edge noise, etc... The project was initiated in 2006 with a pilot experiment during which the high-frequency microphone measurement technique was tested in the VELUX open jet wind tunnel. In 2007, the NACA0015 airfoil (as well as the Risø-B1-18 and Risø-C2-18 airfoils) was equipped with an array of these high-frequency microphones placed on its surface, and was measured in the wind tunnel at LM Glasfiber. An extensive experimental campaign involving several configurations relevant for wind turbine applications (different turbulent inflow conditions, variable inflow velocity and angle of attack, effect of boundary layer devices) was conducted. The experimental data provide a good insight into the flow field over the airfoil. The objective of the present study is to analyze the experimental results with inflow turbulence noise and trailing edge noise as the main focuses. Note that these data were also analyzed in the perspective of boundary layer transition (see Døssing [10]). In a longer perspective, the conclusions drawn from the present study should help to better characterize and/or model turbulent inflow noise and trailing edge noise.

The text is organised as follows. The next section of this report shortly introduces the measurement campaign in the LM Glasfiber wind tunnel, as well as the experimental set-up. In the third section, the hot-wire measurement data are analyzed and used to characterize the inflow turbulence conditions in the wind tunnel. The hot-wire calibration and measurement error analysis are detailed in Appendix A. A short reminder of turbulence theory relevant for this analysis is provided in Appendix B. The fourth section is dedicated to the analysis of measurement data obtained with the airfoil surface microphones. These data are first checked for homogeneity. The actual analysis of the result begins with identification of the potential (additional) sources of sound, which reduces to a study of the data when (almost) no turbulence is present in the incoming flow. An identical analysis of the results is performed, but this time when turbulent inflow is generated by turbulence grids located in the wind tunnel upstream of the airfoil section. In particular, the pressure differences between the suction and the pressure sides at various airfoil plane locations are analyzed in details as these generate the turbulent inflow noise in the far field. The chordwise and spanwise coherence of the pressure fluctuations are finally studied. The model developed by Amiet [1, 2] for expressing the pressure differences as a function of the turbulent inflow characteristics, and which is used in the above-mentioned analysis, is detailed in Appendix C following the development of Mish [20, 18]. In the fifth section, the same data are analyzed, but this time in the perspective of trailing edge noise according to the model developed by Parchen [22] as described in Appendix D. General conclusions are drawn in the last section.

2 Experimental Set-up

2.1 The LM Glasfiber Wind Tunnel

LM Glasfiber's wind tunnel is designed for the testing of wind turbine airfoils [21]. The actual test section dimensions are 1.35 m in width, 2.70 m in height, and 7 m in length. The maximum flow speed of 105 m/s can result in a Reynolds number of 6×10^6 for an airfoil with a 0.9 m chord. Note that the temperature can be kept constant thanks to an automated control system.

The turbulent inflow conditions were controlled by the introduction of turbulence grids with two different solidities and which were placed in the wind tunnel upstream of the airfoil section. The first one, which is denoted as *low solidity* grid, has a 200×200 mm mesh size. The second one, denoted as *high solidity* grid, has a 100×100 mm mesh size. In the absence of grid, a previous study showed that the inflow turbulence intensity is quite small [21]. Hot-wire measurements analysis revealed that it is roughly of the order of $I=0.1\%$ in all velocity directions at all wind tunnel inflow velocities.

During the present campaign, a tri-axial hot-wire anemometer was placed in the wind-tunnel in order to evaluate the inflow turbulence characteristics. An analysis of these results is presented below, indicating that the inflow turbulence in the wind tunnel is substantially higher than the above-mentioned results in the absence of grid.

2.2 Hot-Wire Measurements

Tri-axial sensor probes were purchased from Dantec Dynamics [12] and mounted in the wind tunnel in order to measure the three components of the inflow velocity and analyze the inflow turbulence characteristics. Details of the calibration of the sensors, as well as an error analysis of the resulting velocity components, are provided in Appendix A. The sampling rate of the measurement data is 50 kHz. However, the time response of the hot-wire device limits the effective valid sampling rate to 10 kHz. Nevertheless, this allows for an analysis of relatively small turbulence scales.

Various inflow velocities U_∞ were considered and these are reported in Table 1. The analysis of the measurements with and without inflow turbulence grid are presented in Section 3. Note that the airfoil model was not present in the wind tunnel when these measurements were performed.

U_∞ [m/s]	15.0	26.7	35.1	42.0	50.1	60.1	70.1	80.1	90.1	100.0
Re ($\times10^6$)		1.6			3.0					6.0

Table 1. Inflow Velocities and Associated Reynolds Numbers

2.3 Airfoil Model and Surface Microphones

A NACA0015 airfoil section with a chord $C=0.9$ m and a spanwise extension $L=1.35$ m was installed in the wind tunnel. For each experimental configuration, the angle of attack (corrected for wind tunnel effects) was incrementally modified from $\alpha=-22^o$ to 22^o. Three different inflow velocities were considered in the experimental campaign and the respective Reynolds numbers Re based on the airfoil chord are reported in Table 1 when appropriate. Note that only the clean

surface airfoil conditions (i.e. without the addition of zig-zag tapes that are used to trigger boundary layer transition) are considered here.

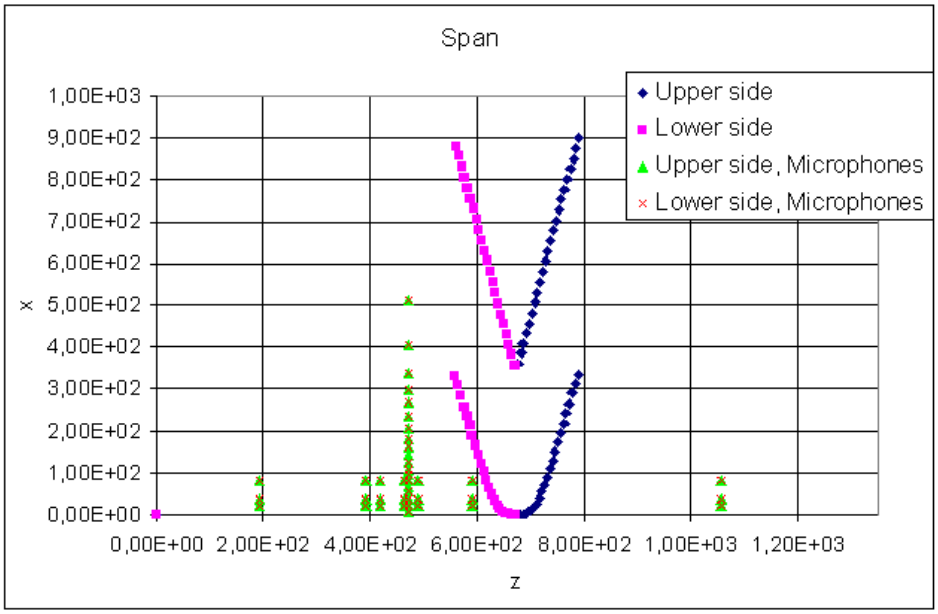

Figure 1. Microphones Locations

The microphones mounted on the airfoil surface have a sampling frequency equal to $f_s = 50\,\text{kHz}$. The array distribution of these microphones is displayed in Fig.1. It consists of 38 microphones placed on the suction side of the airfoil (green triangles). A chord-aligned series of 17 microphones is located at a spanwise location $z/C = 0.33$ allowing for measurements starting near the trailing edge at $x/C = 0.01$, and extending further downstream on the airfoil surface up to $x/C = 0.567$. Additional 7 chord-aligned series of microphones are placed at different spanwise locations: $z/C = 0.02$, 0.24, 0.27, 0.32, 0.35, 0.46 and 0.98, with the microphones located at the following 3 chordwise locations: $x/C = 0.025$, 0.04 and 0.09. An identical number of microphones are symmetrically placed on the pressure side of the airfoil (red crosses), resulting in a total of 76 microphones.

The measured microphone data are used to validate the inflow turbulence model by Amiet [1, 2] in Section 4, and the trailing edge noise model by Parchen [22] in Section 5.

3 Inflow Turbulence

This chapter is dedicated to the analysis of the turbulent inflow conditions in the LM wind tunnel. The measured data collected with the tri-axial hot-wire device which was installed in the wind tunnel (before mounting the airfoil section inside the test section) are presented and analyzed.

The calibration and calculation of the velocity time-series from the hot-wire voltage outputs are described in Appendix A. A brief summary of the techniques that are used to analyze these data are reported in Appendix B. They are mostly based on spectral turbulence theory. The assumptions of homogeneity and isotropy are required to obtain analytical solutions.

Note that the subscripts x, y and z refer to the wind tunnel streamwise and the two transversal flow directions, respectively. The indices 1, 2 and 3 will be sometimes used instead.

3.1 Turbulence Intensity and Length Scales

The above-mentioned techniques are applied to the time-series of the velocity components measured by the hot-wire device. In the figures presented in this section, several sets of averaged inflow velocities are used for calibration and calculation of the velocity time-series. As reported in Table 1, 10 different inflow velocities were considered when performing hot-wire measurements. Since the calibration process requires 5 different averaged inflow velocities, 6 different calibration sets were defined using:

- the 1^{st} to the 5^{th} inflow velocities
- the 2^{nd} to the 6^{th} inflow velocities

$$\vdots$$

- the 6^{th} to the 10^{th} inflow velocities

yielding 6 different curves corresponding to each calibration set in the following figures.

Figures 2(a-b), 2(c-d) and 2(e-f) display turbulent intensities as functions of the inflow velocity when no turbulence grid is present in the tunnel, with the low solidity grid and with the high solidity grid, respectively. It can be observed that there exists an excellent agreement between the two methods of predicting the turbulence intensities I_x and $\widetilde{I}_x$ (see details in Appendix B). However, the turbulence intensities are quite similar for the low and high solidity grid.

Figs.3(a-b), 3(c-d) and 3(e-f) display the integral length scales Λ_x as defined in Section B.1 and $\widetilde{\Lambda}_x$ as defined in Eq.(B.8) as functions of inflow velocity for the same cases. There is a general good agreement between the two methods for the cases with turbulence grid, but there exist substantial discrepancies without grid, in particular at velocities below 70 m/s. The procedure used to calculate the integral with infinite bound in Eq.(B.2) can cause evaluation errors when defining Λ_x. The evaluation of $\widetilde{\Lambda}_x$ is therefore more reliable. Small differences are observed between the low and high solidity grids.

Figs. 4(a-b), 4(c-d) and 4(e-f) display similar results for the dissipation length scales η_x and $\widetilde{\eta}_x$. The agreement is again very good for the cases with turbulence grid, but some discrepancies appears without grid, again at lower velocities. Small differences are observed between the low and high solidity grids.

The analysis is continued by looking at the influence of the different directions on the calculated quantities. Only the turbulence intensities and the integral length

scales are considered. The data obtained by fitting the measurements to the theoretical Von Karman spectrum are displayed in Figs.5(a-b-c) for the turbulence intensities and in Figs.6(a-b-c) for the integral length scales.

It can be seen the turbulence intensities are higher for the transversal components for the case without grid, but they are of the same order as the streamwise component when the grids are present.

Without grid, the integral length scales are slightly larger for the transversal components. When grids are present, the transversal and streamwise components yield similar integral length scales at low inflow velocities, but as the velocity increases, these scales for both transversal components suddenly drop to lower values while the streamwise component's scale remain of the same order.

The above calculated turbulent intensities for the case without turbulence grid (see Fig.5(a)) are substantially higher than those evaluated in the same wind tunnel as reported in the study performed during its aerodynamic commissioning [21]. Indeed, in the latter study turbulent intensities of the order of $I = 0.1\%$ were measured with a hot-film device at inflow velocities equal to 50, 80 and 100 m/s. These measurements did not include fluctuations below 10 Hz. In the present study, the following values of the turbulent intensity were evaluated for the same inflow velocities: $I = 0.46, 1.04$ and 1.48%, respectively. The last value might be slightly erroneous as it is located at the end of the calibration scale. Removing the lower part of the spectra (< 10 Hz) did not significantly modify these results.

Assuming that there exist large measurement errors on the transversal components and only considering the streamwise component, the turbulence intensities estimated in this study: $I_x = 0.26, 0.58$ and 0.82%, still remains substantially higher than those from the commissioning study. The cause of these discrepancies remains unclear.

Since small differences were observed between results obtained for the low and high solidity grids, only those obtained with the high solidity grid are considered in the remaining of this section (and in some other sections of this report).

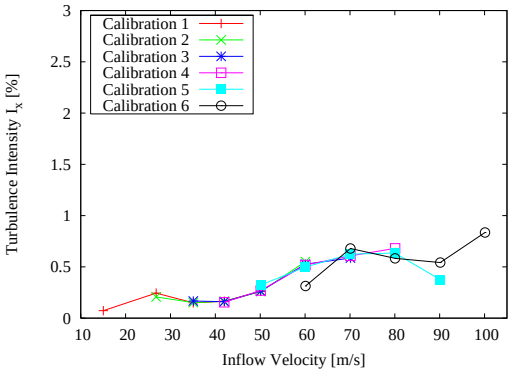

(a) I_x - No turbulence grid

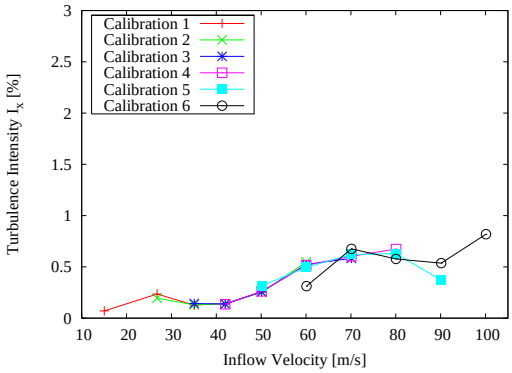

(b) $\widetilde{I}_x$ - No turbulence grid

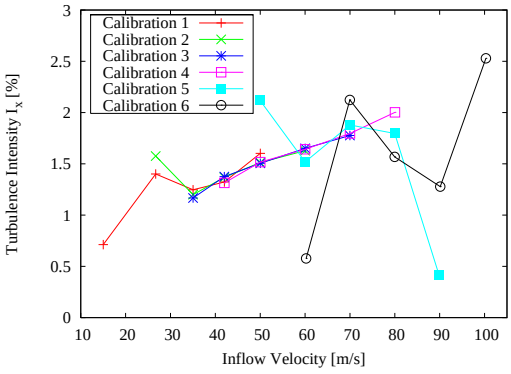

(c) I_x - Low solidity grid

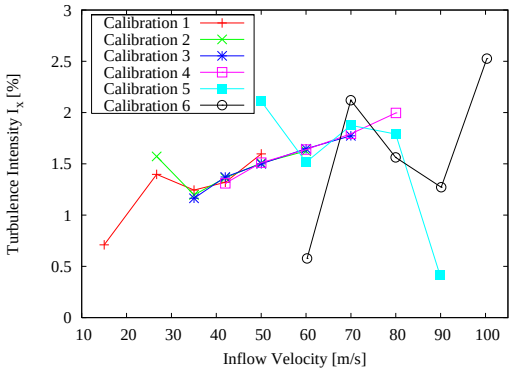

(d) $\widetilde{I}_x$ - Low solidity grid

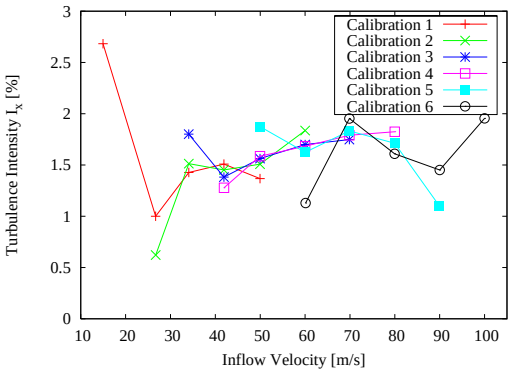

(e) I_x - High solidity grid

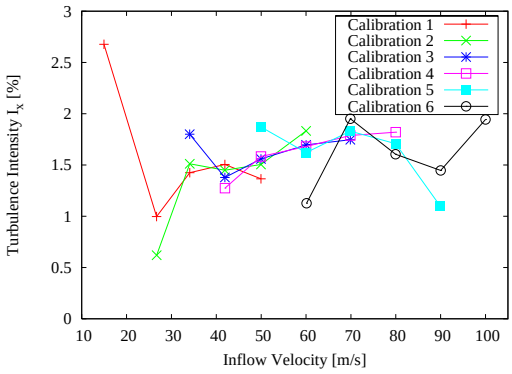

(f) $\widetilde{I}_x$ - High solidity grid

Figure 2. Turbulence Intensity

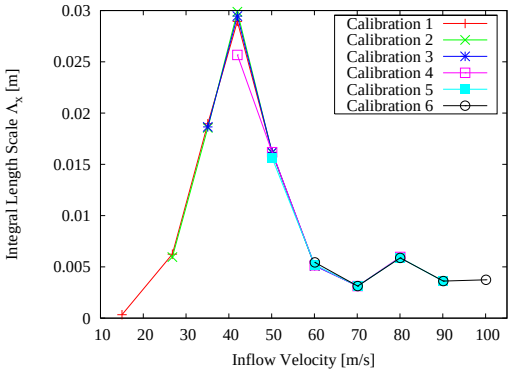

(a) Λ_x - No turbulence grid

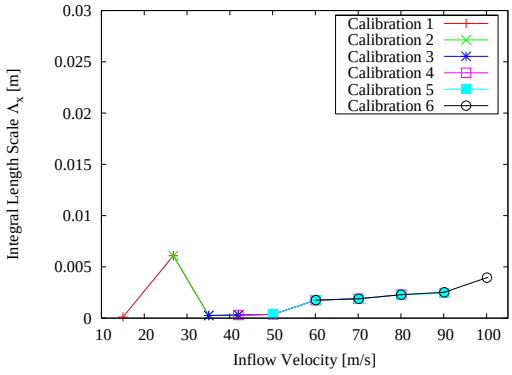

(b) $\widetilde{\Lambda}_x$ - No turbulence grid

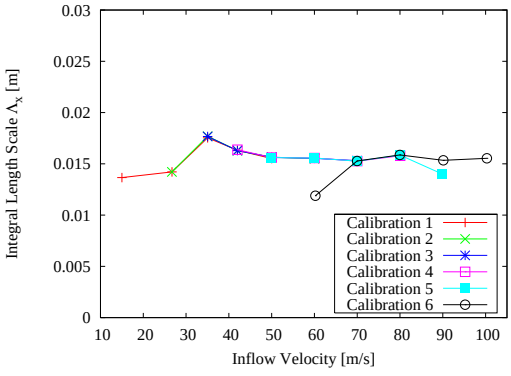

(c) Λ_x - Low solidity grid

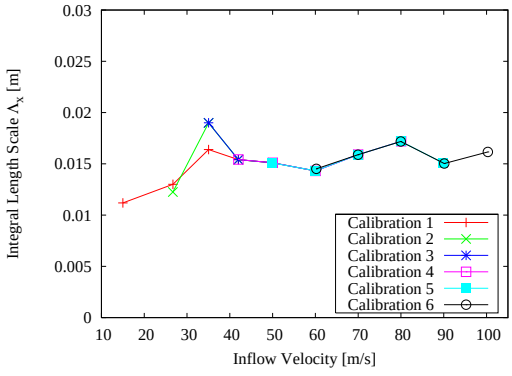

(d) $\widetilde{\Lambda}_x$ - Low solidity grid

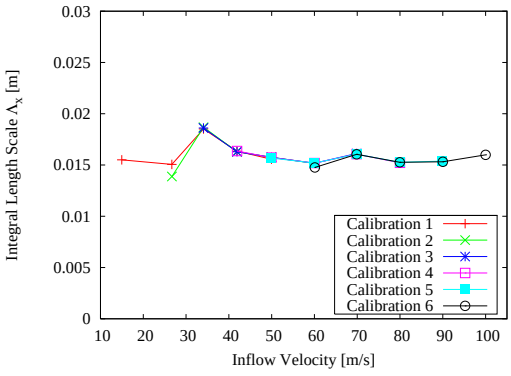

(e) Λ_x - High solidity grid

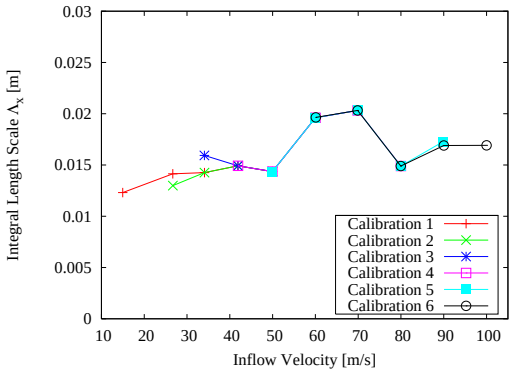

(f) $\widetilde{\Lambda}_x$ - High solidity grid

Figure 3. Integral Length Scale

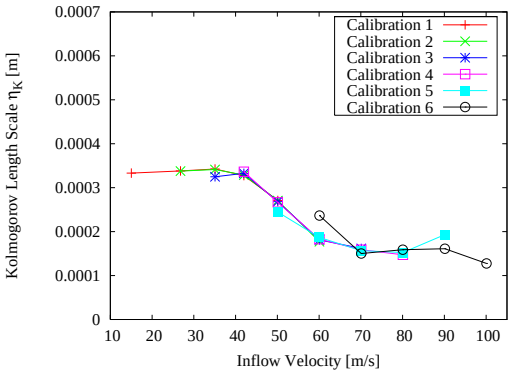

(a) η_K - No turbulence grid

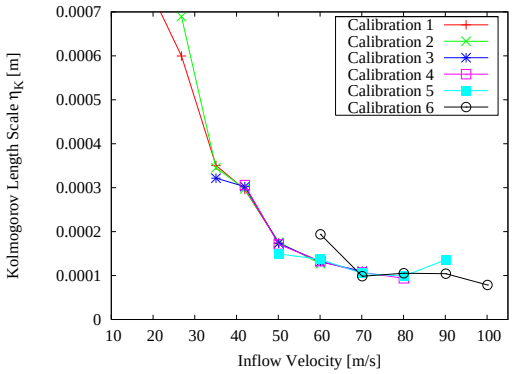

(b) $\widetilde{\eta}_K$ - No turbulence grid

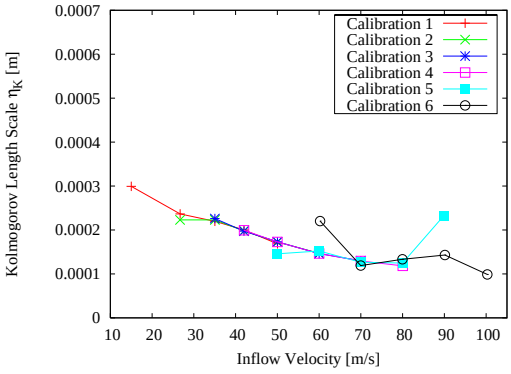

(c) η_K - Low solidity grid

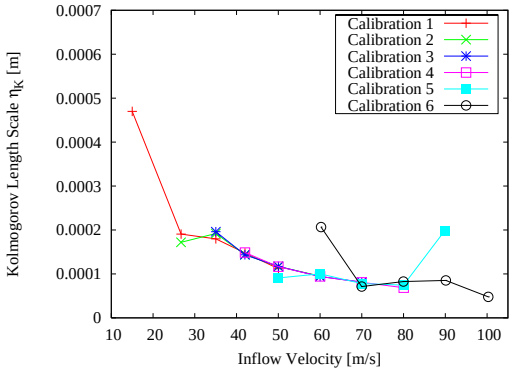

(d) $\widetilde{\eta}_K$ - Low solidity grid

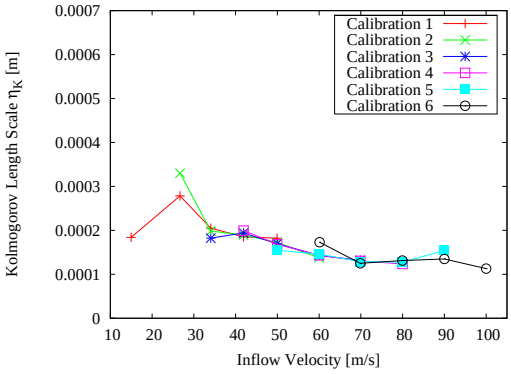

(e) η_K - High solidity grid

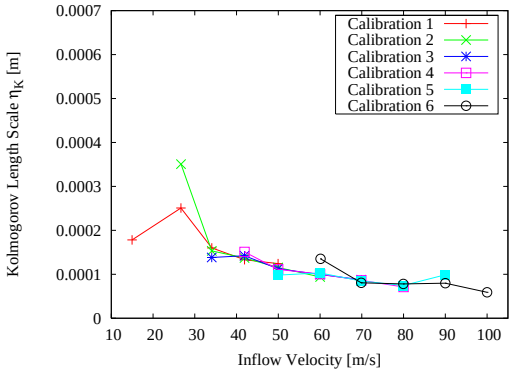

(f) $\widetilde{\eta}_K$ - High solidity grid

Figure 4. Kolmogorov Dissipation Length Scale

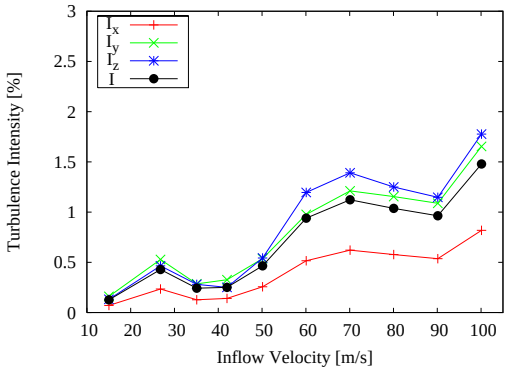

(a) No turbulence grid

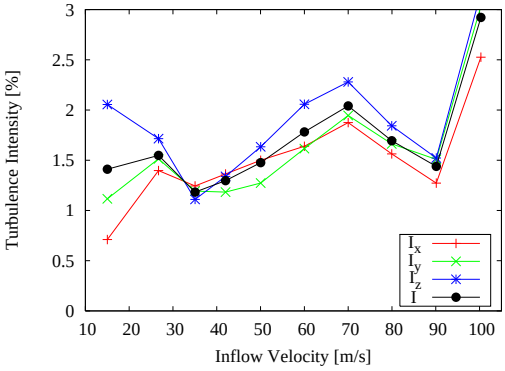

(b) Low solidity grid

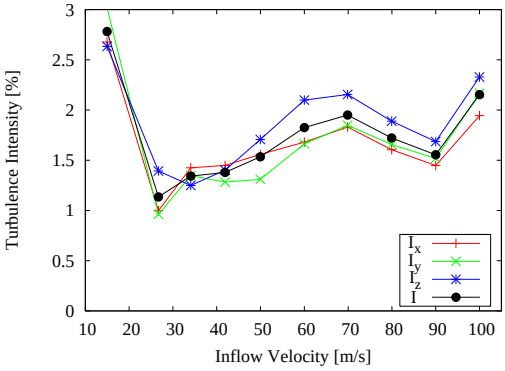

(c) High solidity grid

Figure 5. Turbulence Intensities $\widetilde{I}, \widetilde{I}_x, \widetilde{I}_y, \widetilde{I}_z$

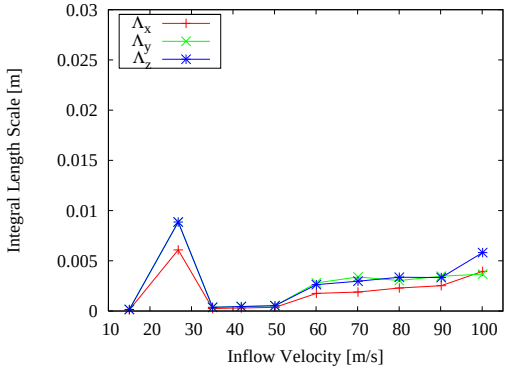

(a) No turbulence grid

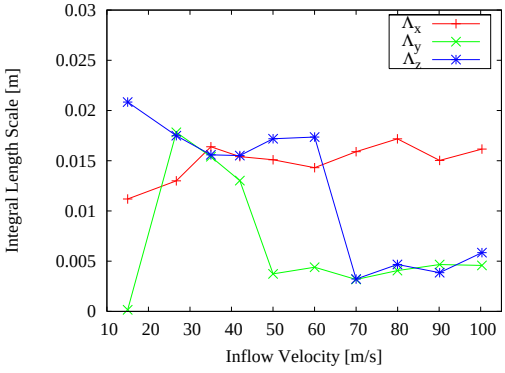

(b) Low solidity grid

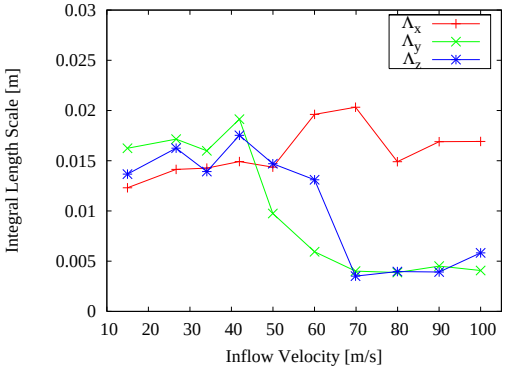

(c) High solidity grid

Figure 6. Integral Length Scales $\widetilde{\Lambda}_x, \widetilde{\Lambda}_y, \widetilde{\Lambda}_z$

3.2 Analysis of One-Point Spectra

The one-point spectra pre-multiplied by the wavenumber k_1 are displayed in Figs.7(a) and (b) for the cases without turbulence grid and with the high solidity grid, respectively. On these figures, both the experimental and the theoretical Von Karman spectra are reported. The latter ones are constructed by using the velocity variances and integral length scales that were evaluated by averaging the time-series and calulating the auto-correlation functions, respectively, instead of using the data that were obtained by fitting the theoretical spectra to the experimental ones. This explains the discrepancies in the maximum location of the spectra in these figures.

Concerning the measured data in the case without turbulence grid, it is quite clear that there does not exist any isotropic inertial subrange characterized by the classical $-5/3$ slope of the one-point spectra (or $-5/3+1=-2/3$ slope of the pre-multiplied spectra). The $+1$ slope at low wavenumbers is characteristic of large turbulent scales, but also of a white noise signal. Considering the fact that no inertial subrange exists and that the energy levels are lower in this case than in the case with turbulence grid (see below), it could be that the measured signals are only residual noise from the instruments and that the turbulence level in the wind tunnel is quite low. At higher wavenumbers, all experimental spectra suddenly plunge with a constant steep slope towards low energy levels. Since this plunge initiates at the same wavenumber $k_1 \approx 500\,\mathrm{m}^{-1}$ at all velocities both in the case with and without turbulence grid, this indicates that the limit of the time response of the hot-wire has been reached.

Concentrating now on the spectra obtained with the high solidity grid, it can be observed that the measured spectra for the streamwise component all present a wavenumber range with a $-2/3$ slope similar to the inertial subrange of the theoretical Von Karman spectrum. At lower wavenumbers the $+1$ slope characteristic of large turbulent scales is also recovered. In addition, the calculated input data (velocity variances and integral length scales) used for plotting the theoretical spectra yield to a very good agreement compared to the measured spectra (for wavenumbers below the one where the experimental spectra begin to roll-off). Contrastingly, the experimental spectra are quite unexpected when looking at the transversal components. Except for the two first wind-tunnel averaged velocities ($U_\infty = 26.7$ and $50.1\,\mathrm{m/s}$) for which an inertial subrange $-2/3$ slope can be observed, the two other cases present a subrange for which the spectra continue to increase as a function of the wavenumber after the initial lower wavenumbers $+1$ slope region, but with a smaller slope. To the best author's knowledge, this does not correspond to any physical turbulence theory. This might originate from the so-called 'bottleneck' phenomenon that occurs in ducts (here the duct being the wind-tunnel section itself), but this should in this case also be observed for the streamwise component. It might also originate from the larger amplification errors of the transversal components mentioned earlier.

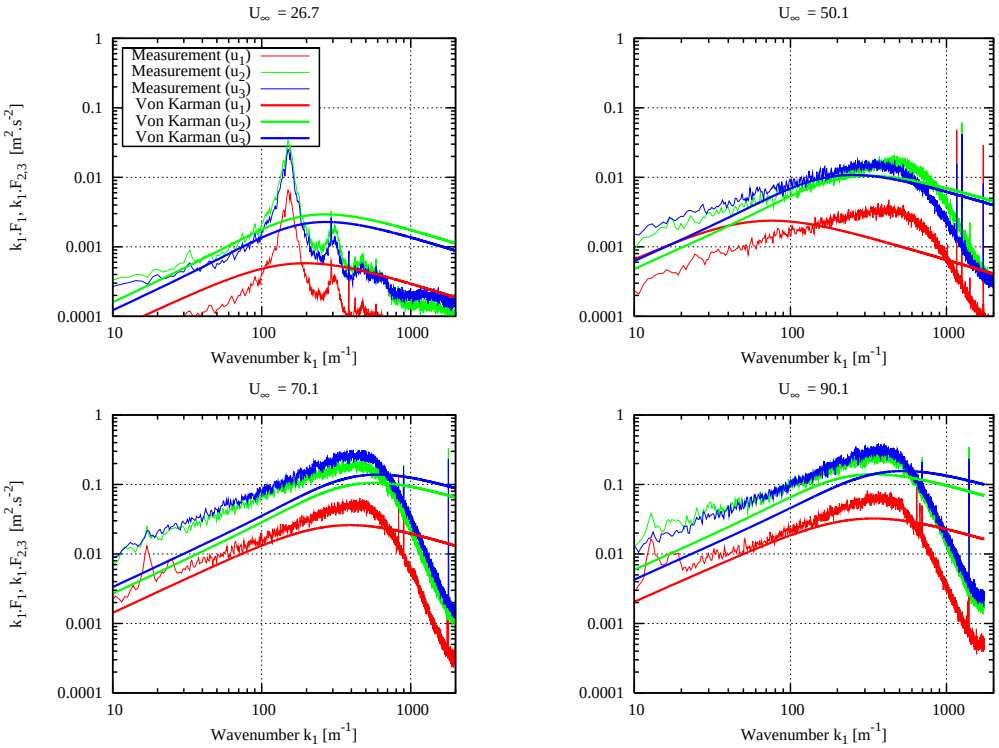

(a) No turbulence grid

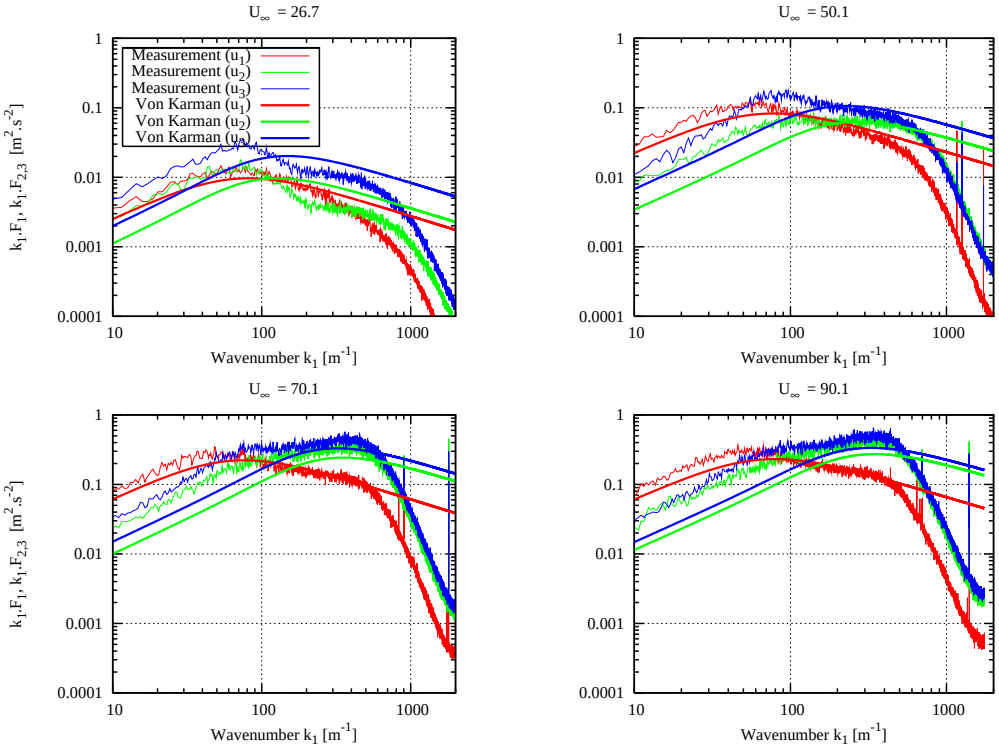

(b) High solidity grid

Figure 7. Pre-Multiplied One-Point Velocity Spectra

3.3 Komogorov Length Scale and Dissipation

To confirm the existence of an inertial subrange from the one-point velocity spectra, Champagne [7] suggests to plot the ratios between the transversal velocity components spectra and the streamwise velocity spectrum. Assuming isotropy, these ratios should theoretically approach a 4/3 constant value within the inertial subrange. These ratios are displayed as functions of wavenumber in Figs.8(a) and (b) for the cases without turbulence grid and with the high solidity grid, respectively. In the former case, the ratio is much larger than 4/3 for the whole frequency domain. This may indicate that the noise to signal ratio is quite high for both transversal components. In the latter case for $U_\infty = 50.1\,\mathrm{m/s}$, the ratio for the u_3-component seems to stabilize in the wavenumber range $k_1 = 100$ to $300\,\mathrm{m}^{-1}$. However, the ratio approaches a value of 2 slightly higher than the 4/3 theoretical value. A somehow constant value of the ratio is also observed for the first wind tunnel velocity. In the other cases, a constant ratio is never observed. One of the possible reasons for this is the fact that the transversal components are too corrupted by measurement noise as mentioned above, therefore masking the possibly existing isotropic inertial subrange. Nevertheless, the fact that the turbulence in the wind tunnel is far from being isotropic remains a possibility.

Finally, the dissipation rates calculated according to Equation (B.11) are plotted in Figs.9(a) and (b) for the cases without turbulence grid and with the high solidity grid, respectively. As expected, in the former case there does not exist a clear range for which the calculated dissipation rate stabilizes at a constant value. In the latter case, such a subrange is clearly observed in the case $U_\infty = 50.1\,\mathrm{m/s}$. For the first inflow velocity, the inertial subrange might be existing, but the dissipation remains quite small compared to the other cases. For the two highest inflow velocities, after the negligeable values at low wavenumbers the dissipation rate grows up to a level equivalent to the case $U_\infty = 50.1\,\mathrm{m/s}$, but continues thereafter to slowly increase until the maximum temporal resolution of the hot-wire is reached.

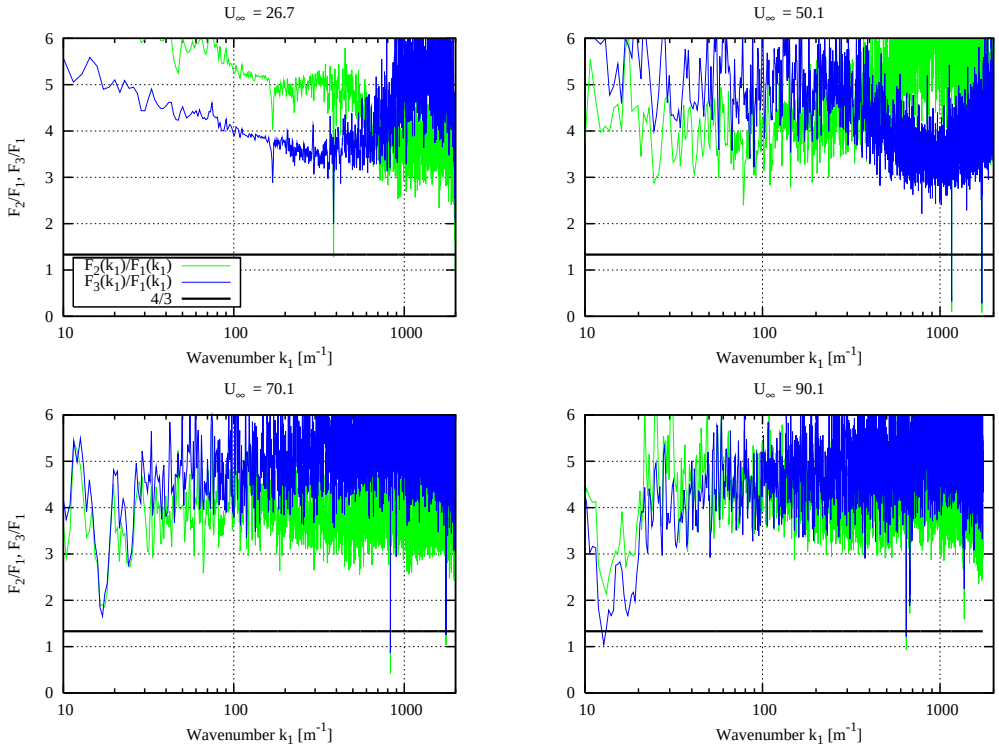

(a) No turbulence grid

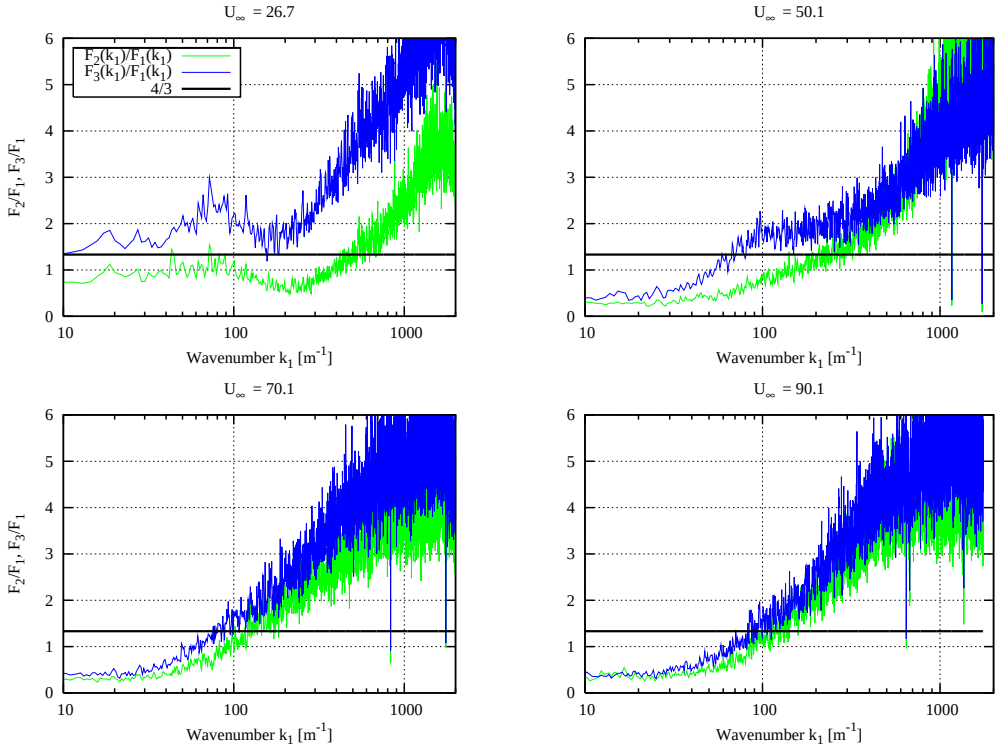

(b) High solidity grid

Figure 8. Transversal to Streamwise One-Point Velocity Spectra Ratios

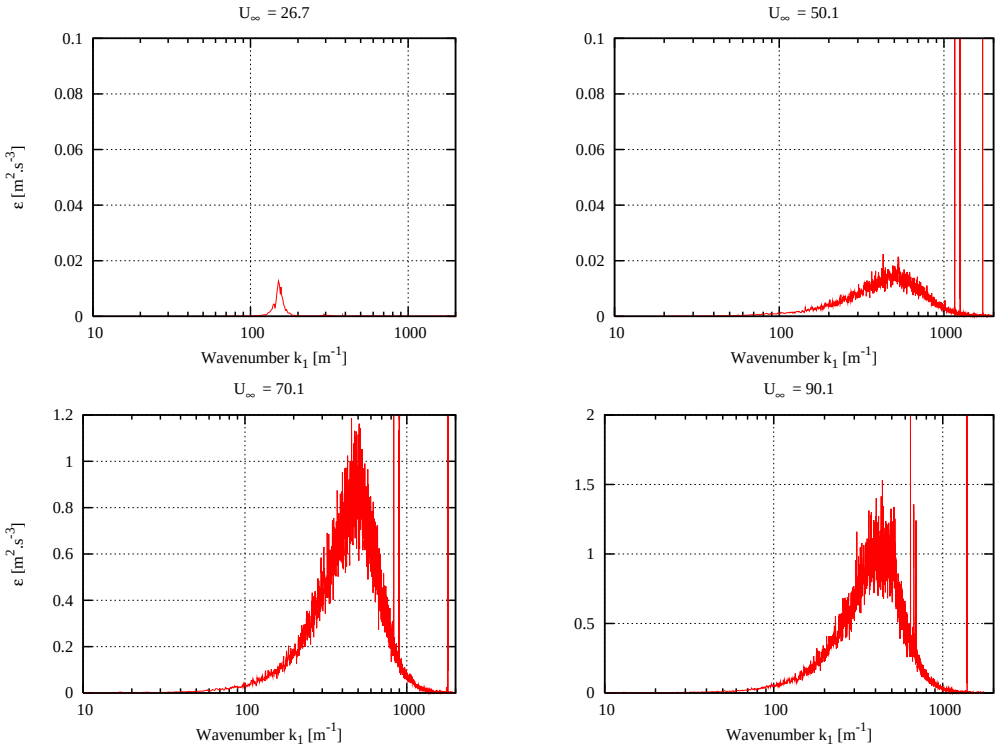

(a) No turbulence grid

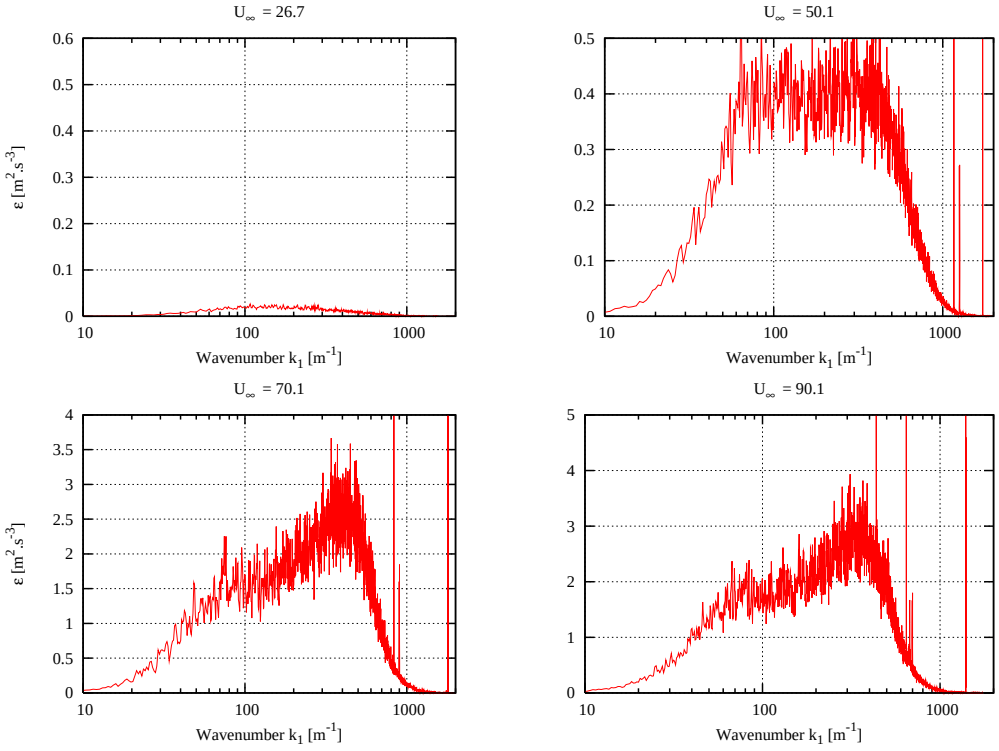

(b) High solidity grid

Figure 9. Spectrum of the Dissipation Rate

4 Turbulent Inflow Noise

In this section, the data measured with the microphones placed on the airfoil section surface are analyzed in the perspective on inflow turbulence noise. All data presented in this section are concerned witht the wind tunnel inflow velocity $U_\infty = 26.7\,\mathrm{m/s}$, resulting in a Reynolds number based on the airfoil chord equal to $Re = 1.6 \times 10^6$.

4.1 Homogeneity Check

The microphones measurement data are analyzed in a few configurations in order to evaluate their global validity. The data processing methodology that will subsequently be used to correct some of these data for further analysis is introduced.

It should first be noted that the time-series measured by any pair of microphones located on the same side of the airfoil and at the same chordwise location should have the same statistical properties. This should hold irrespectively of the flow configuration. Indeed, assuming that the incoming flow is relatively homogeneous across the wind tunnel section as it was proved in the wind tunnel commissioning study [21], together with the fact that the airfoil section is identical along its span, should induce spanwise homogeneity of the measured pressure fluctuations on the surface of the airfoil. The objective of this section is to validate this assumption. Note however that end wall effects at the extremities of the airfoil section may significantly alter this homogeneity in the vicinity of these walls.

At an angle of attack $\alpha = 0^o$, in addition to the spanwise homogeneity, the symmetry of the NACA0015 airfoil itself should yield statistically identical results on both sides of the airfoil at a given chord location.

Defectuous Microphones

The case with no turbulence grid and for an angle of attack $\alpha = 0^o$ is considered first. Fig.10(a) displays the original power spectra of the surface pressure fluctuations measured by various microphones as a function of the frequency f. Each plot contains data obtained at a specified chordwise location either on the suction or the pressure side of the airfoil, and displays the power spectra obtained at all spanwise locations. As mentioned above, each plot should exhibit nearly identical power curves. In addition, plots corresponding to the same chordwise location on the suction or the pressure side should as well exhibit identical power curves since $\alpha = 0^o$. However, it can be seen that this is not always the case. Some curves significantly diverge from the other ones, as for example for some of the microphones at $x/C = 0.025$ on the pressure side, or $x/C = 0.09$ on the suction side. These discrepancies are not restricted to this particular configuration, but can also be observed for the same microphones at the same angle of attack $\alpha = 0^o$ but in the presence of the high solidity grid in Fig.11(a), or at an angle of attack $\alpha = 20^o$ with the high solidity grid in Fig.12(a). As expected, in the latter case the symmetry between the suction and pressure sides is lost.

Correction Methodology

These discrepancies are attributed to some miscalibrations or faults inherent to the microphones themselves. As observed in the figures mentioned above, it seems that the errors are uniformely distributed across the whole power spectra. Therefore, as a simple remedy it is proposed to correct the faulty time-series by simply multiplying them by a constant such that the expected symmetries are recovered in the power spectrum plots. The correcting multiplicative constants

are initialized for defectuous microphones in the case $\alpha = 0^o$ with the high solidity grid. The corrected power spectra are displayed in Fig.11(b). A relative good symmetry of the results is recovered.

In order to verify that our correction methodology is universal, the same corrections as applied above (i.e. the multiplicative constant used above for one particular defectuous microphone is identically used for the different measurement cases) are applied to the measurement data obtained at $\alpha = 0^o$ with no turbulence grid, and data obtained at $\alpha = 20^o$ with high solidity grid. The corrected power spectra are displayed in Figs.10(b) and 12(b), respectively. As it can be seen, a relative good symmetry is recovered for all the data proving that our correction methodology is satisfactory. However, in some cases some discrepencies remain for higher frequencies beyond 5 kHz, but this frequency range is not of interest for the present study.

In the following of this document, all measurement data that will be used for subsequent derivations and analysis will be checked in a similar way, and corrected if necessary. The results with corrected data will always be shown.

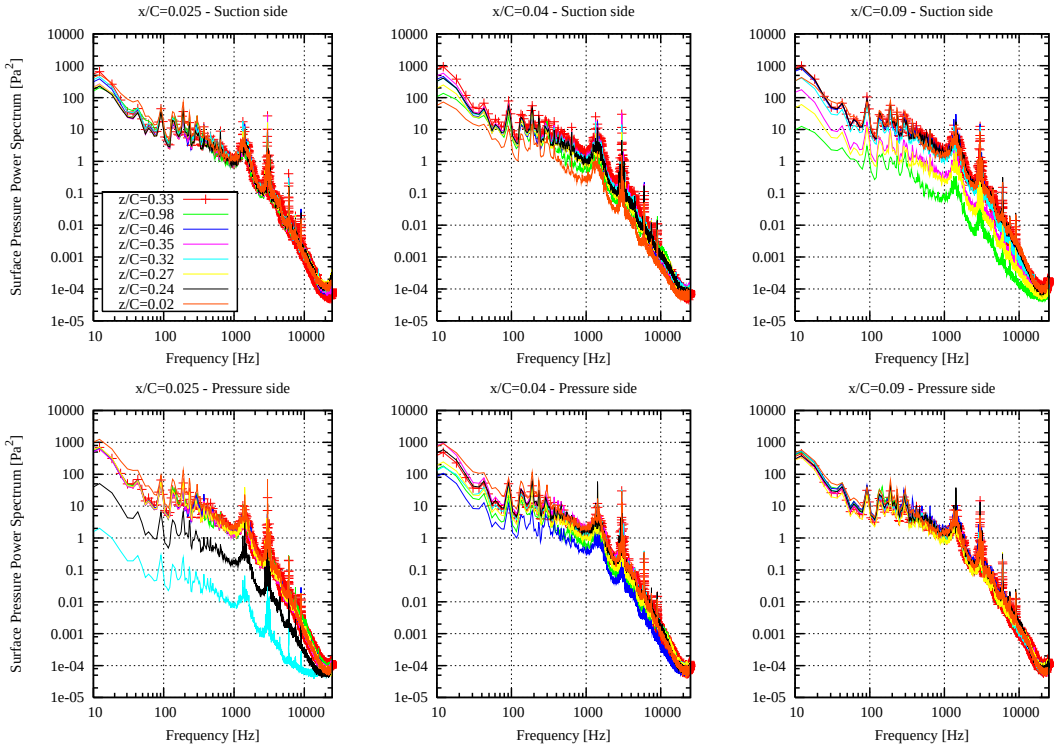

(a) Non-corrected data

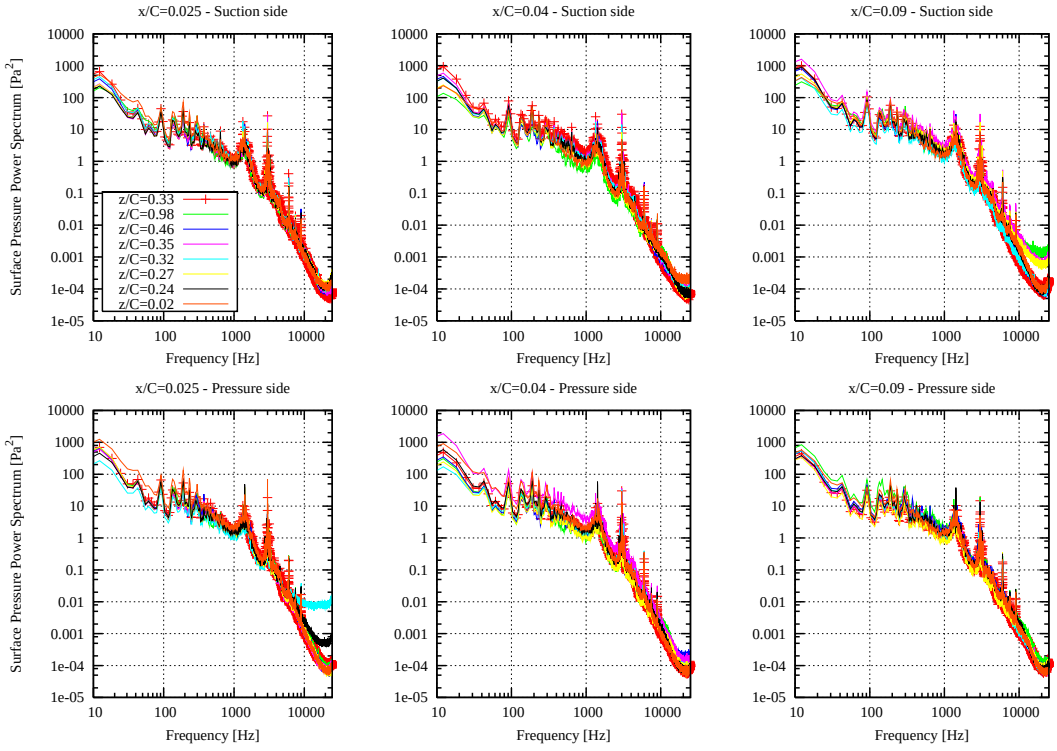

(b) Corrected data

Figure 10. Homogeneity Check - $\alpha = 0^o$ - No Turbulence Grid

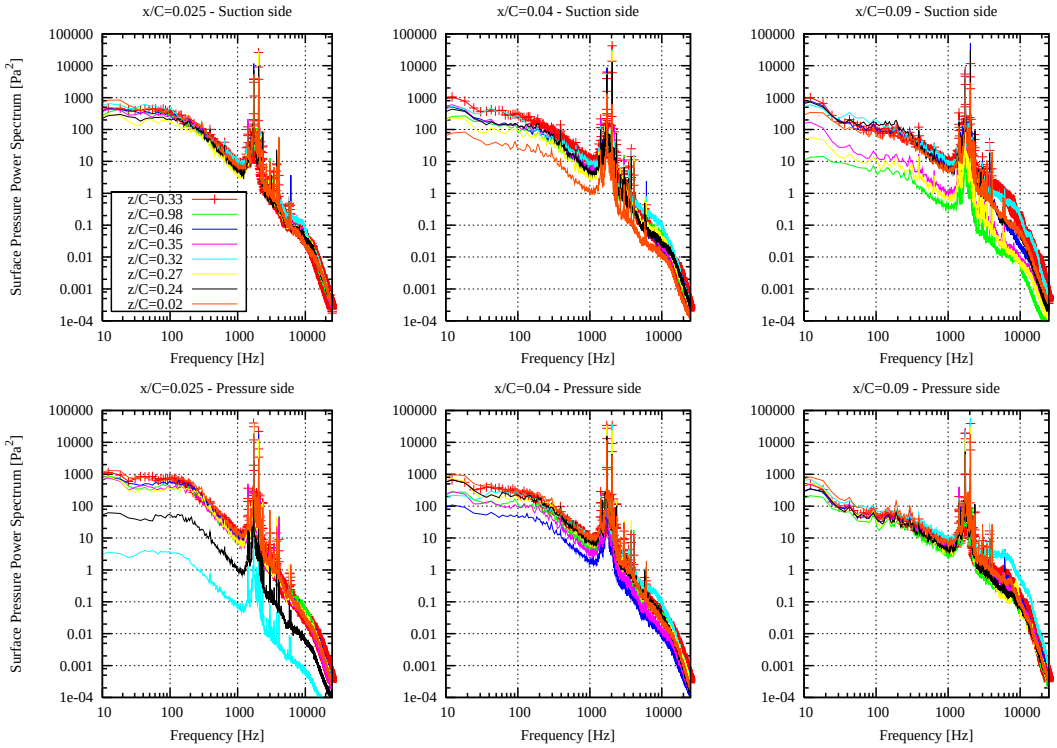

(a) Non-corrected data

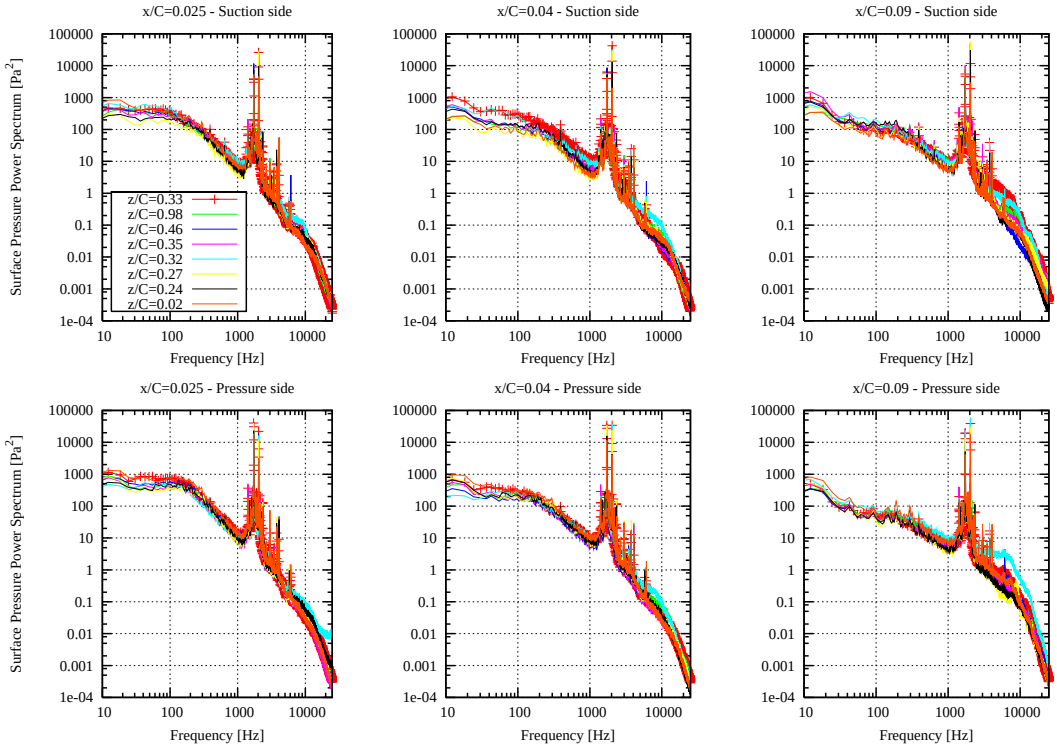

(b) Corrected data

Figure 11. Homogeneity Check - $\alpha = 0^o$ - High Solidity Grid

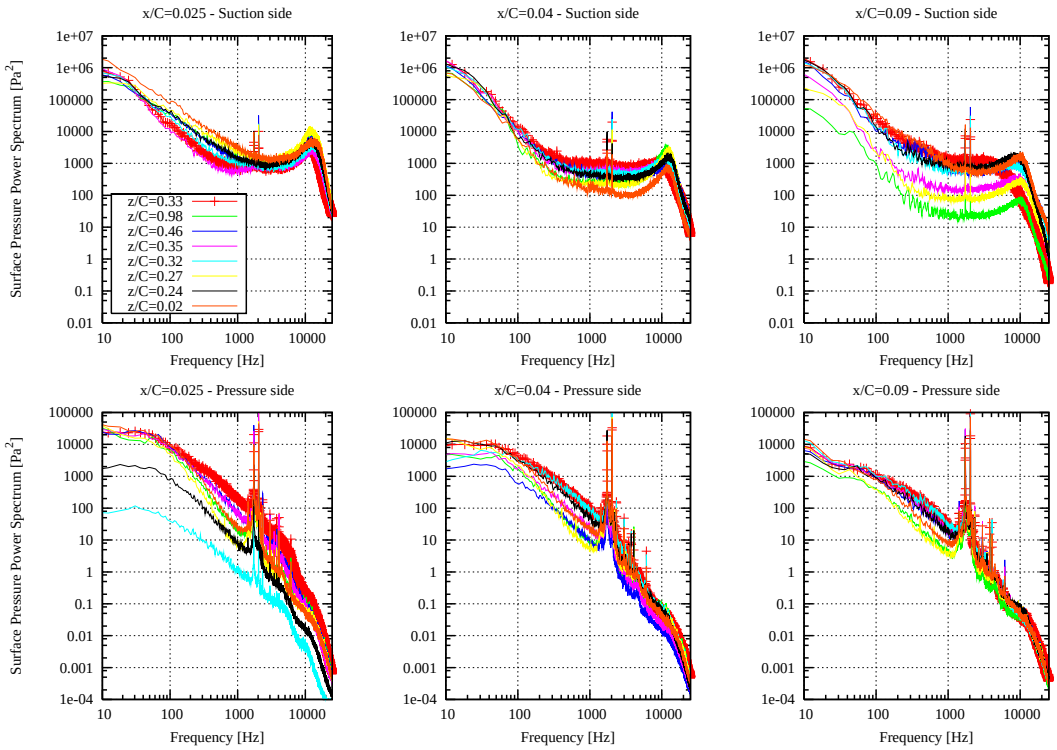

(a) Non-corrected data

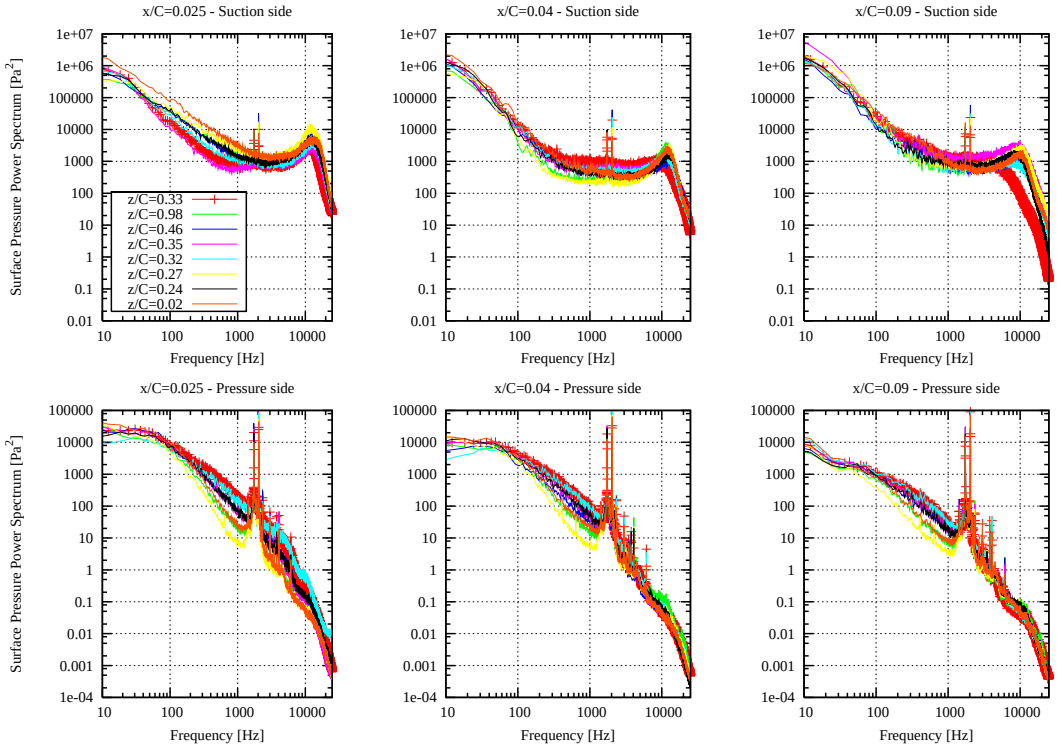

(b) Corrected data

Figure 12. Homogeneity Check - $\alpha = 20^o$ - High Solidity Grid

4.2 Sources of Noise

The goal of this section is to identify the possible polluting noise sources present in the wind tunnel. Indeed, as far as aero-acoustic noise is concerned, the pressure fluctuations on the airfoil surface where the measuring microphones are located can be generated by various mechanisms that can potentially dominate and/or interact with our main focus, namely turbulent inflow noise. Pressure fluctuations on the airfoil surface can for example originate from: acoustic fields generated elsewhere in the wind tunnel section, boundary layer turbulence, stall or boundary layer separation generated eddies convected by the flowfield, etc... The data that will be analyzed in this section originate from measurements for which no turbulence grid is present. Indeed, in this case the inflow turbulence intensity is very weak (of the order of 0.1% [21]). It is therefore expected that potential noise sources that may pollute the turbulent inflow noise can be brought to light.

Cross-spectral analysis can in principle remove the turbulent boundary layer noise effects by using microphones which separation length is greater than the dominant boundary layer turbulence length scale. In our case, pressure differences between the pressure and suction sides of the airfoil are studied. Therefore, it is expected that the effects of boundary layer turbulence are removed from the analyzed spectra.

Experimental Data

For this study, four angles of attack are considered: $\alpha = 0$, 8, 16 and 20^o, for their respective different flow patterns. Lift and drag characteristics as a function of the angle of attack (corrected for wind tunnel effects) are plotted in Fig.13. The averaged pressure distributions on the airfoil at the 4 considered angles of attack are displayed on Fig.14.

In the first case, the flow around the airfoil remains attached on both sides of the airfoil (except may be in the vicinity of the trailing edge if the adverse pressure gradient is too intense), and symmetry of the data between the pressure and suction sides is ensured. In the second case, the flow is still attached on the suction side of the airfoil (at least most of it), but the symmetry between pressure and suction sides is lost. In the third case, the flow separates at some chordwise location on the suction side, although full stall has not been reached yet. In the last case, stall is fully developed and the flow is separated over the whole airfoil suction side.

The sources of noise are analyzed through the auto-spectra of the pressure differences (between pressure and suction sides) at several chordwise locations along the airfoil as plotted in Figs.15(a) and 16(a), and through the coherences and phase differences between the pressures measured on the suction and pressure sides of the airfoil at the corresponding locations as plotted in Figs.15(b) and 16(b). Note that Fig.15 displays the data measured at $x/C = 0.01$, 0.025, 0.04 and 0.06, whereas Fig.16 displays the data measured at $x/C = 0.09$, 0.14, 0.2 and 0.3. These data are plotted as a function of the reduced frequency defined as:

$$\omega_r = \pi C f / U_\infty$$

where f is the frequency in Hertz.

Analysis of Results

Stall

The first noticeable pattern is the high values of the auto-spectra for angles of attack at and beyond stall ($\alpha = 16$ and 20^o) which can be observed at low frequencies ($\omega_r < 7$) for all chordwise stations. This is attributed to the stall phenomenon

which is characterized by the shedding and convection of large vortices in the wake of the airfoil. This vortices generates large amplitude pressure fluctuations which can be felt in the whole neighbourhood of the airfoil, and in particular by the microphones on the airfoil surface.

Transition

A second clear pattern is the sudden increase of spectral energy at all higher frequencies than the one mentioned above (i.e. $\omega_r > 7$), and which only occurs at and downstream of the chordwise station $x/C = 0.06$ for $\alpha = 8^o$, at $x/C = 0.025$ for $\alpha = 16$ and $\alpha = 20^o$ (Note that the shapes of the spectra are somehow different for the two latter angles of attack at that particular station, but become similar again downstream of this point). This pattern originates from the transition to turbulence of the airfoil surface boundary layer, which is a consequence of the rapid acceleration of the flow passing around the leading edge of airfoil. This acceleration is indeed amplified as the angle of attack increases. As observed on the coherence plots, the sudden increase of spectral energy of the pressure differences coincides with a complete loss of coherence between the pressures on both sides of the airfoil, which is expected since the turbulent pressure fluctuations generated by transition on the suction side of the airfoil are totally uncorrelated with the pressure on the pressure side (where the flow may actually remain laminar). Note that this energy increase does not occur at 0^o angle of attack for all considered chord locations indicating that transition do or might occur downstream of the furthest downstream chord location $x/C = 0.3$.

Separation

The last noticeable event is the occurrence of an energy peak in the frequency range $0.7 < \omega_r < 30$ for chordwise stations at and downstream of $x/C = 0.3$ for $\alpha = 16^o$, and $x/C = 0.2$ for $\alpha = 20^o$. As observed on the pressure distributions in Figs.14(c-d), this most certainly originates from the boundary layer separation and subsequent detached flow region on the suction side of the airfoil related to the occurence of stall.

Preliminary Conclusions

From the previous analysis, some conclusions concerning the potential acoustic sources in the wind tunnel can be drawn.

The low pressure difference spectral levels at low angles of attack indicate that inflow turbulence/airfoil interaction will dominate among all the potential acoustic sources in the flowfield in similar configurations (i.e. at low angle of attack, clean airfoil surface, etc...).

At higher angles of attack, larger pressure difference spectral energies due to the occurence of stall are expected to dominate the surface pressure fluctuations and thereby the radiated noise in the farfield.

Transition was found to have an impact on the pressure difference spectra, which was restricted to higher frequencies. Therefore, it may not interact with the turbulent inflow noise sources that are characterized by lower frequencies.

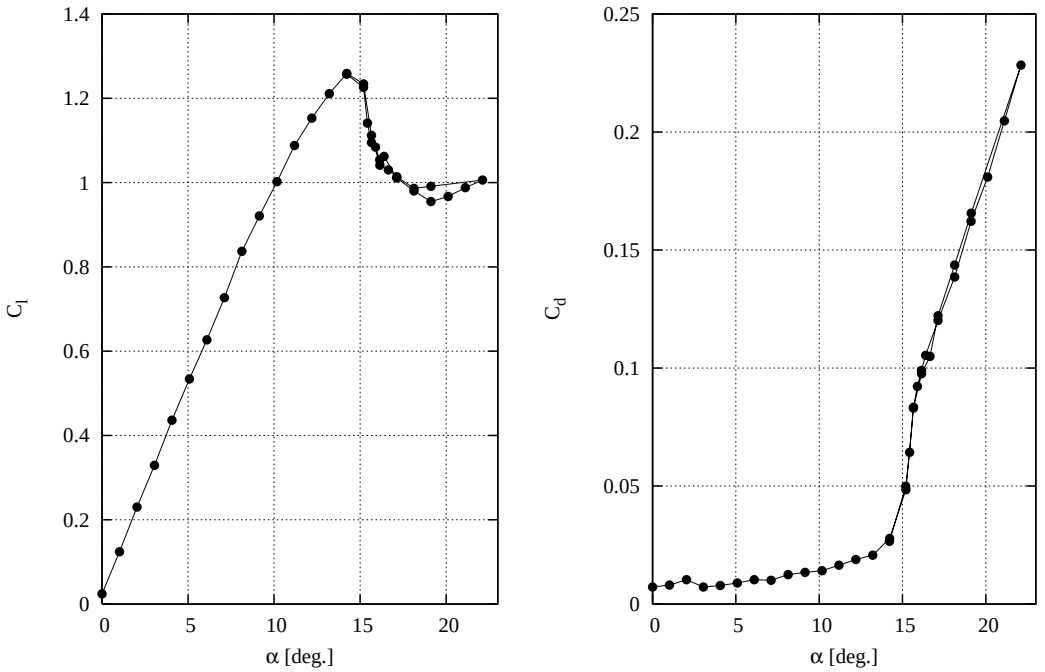

(a) Lift Coefficient (b) Drag Coefficient

Figure 13. Polar Characteristics - No Turbulence Grid

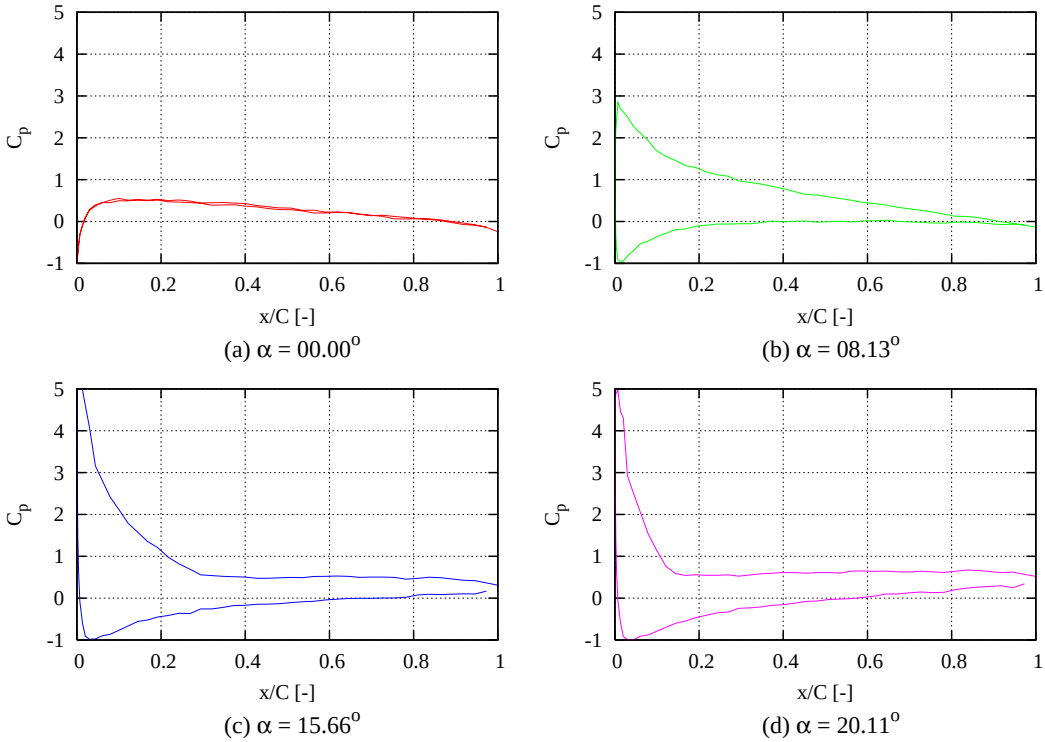

(a) α = 00.00° (b) α = 08.13°

(c) α = 15.66° (d) α = 20.11°

Figure 14. Pressure Coefficient Distributions - No Turbulence Grid

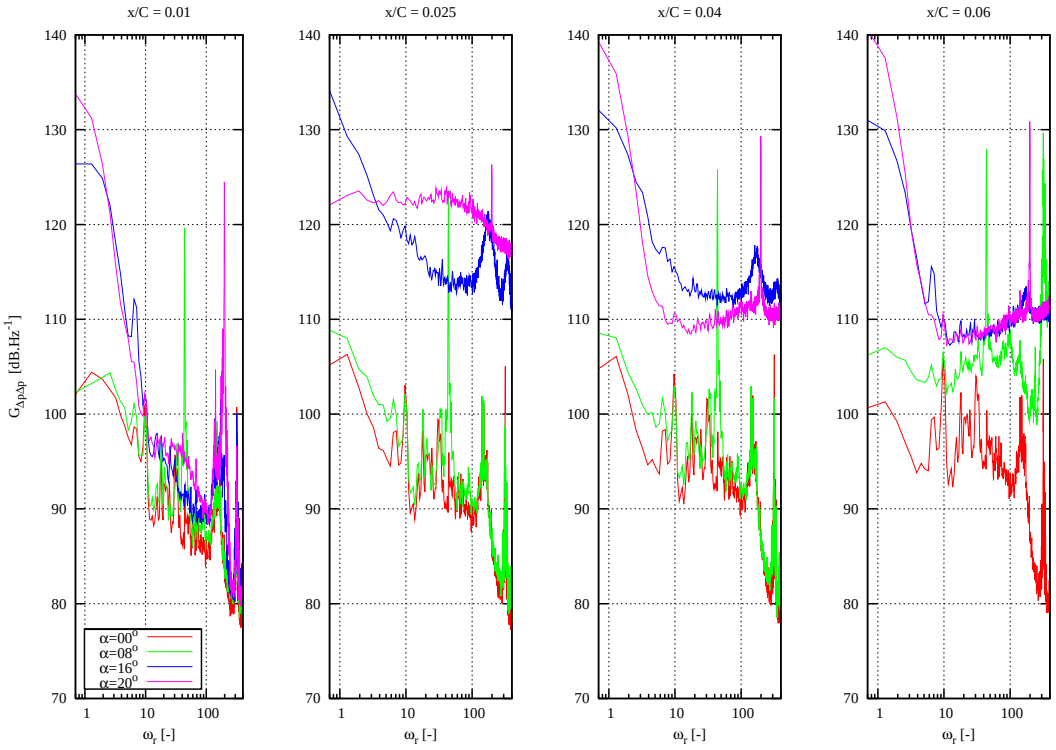

(a) Auto-spectrum of pressure difference

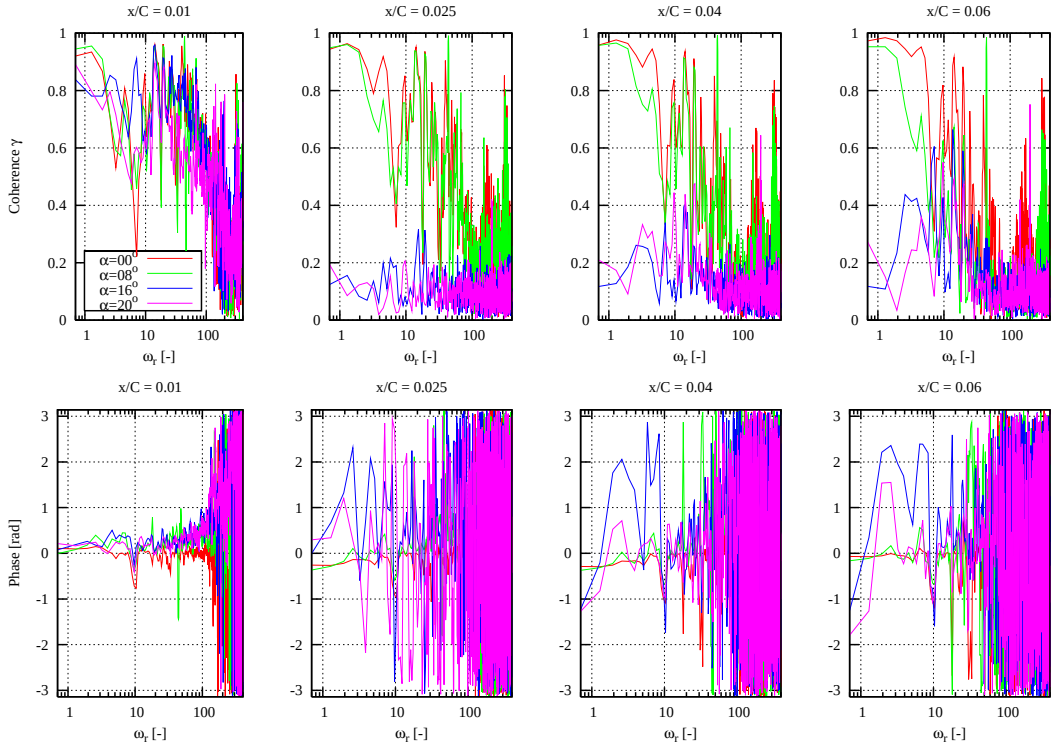

(b) Coherence and phase

Figure 15. Pressure Differences - No Turbulence Grid - x/C=0.01, 0.025, 0.04, 0.06

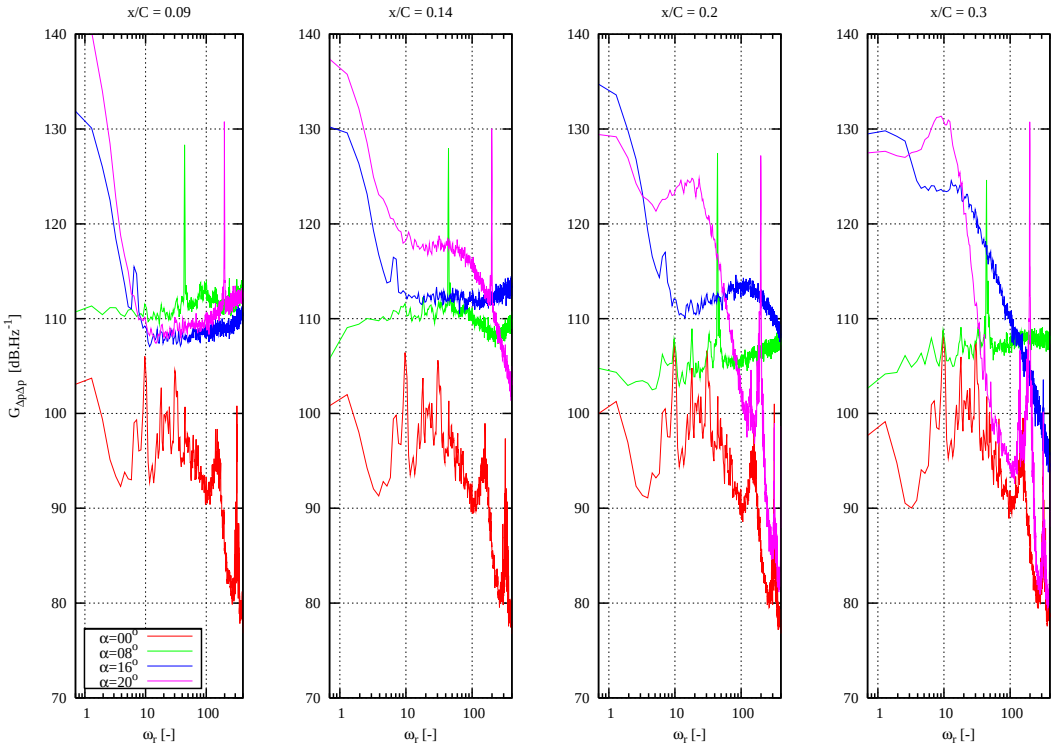

(a) Auto-spectrum of pressure difference

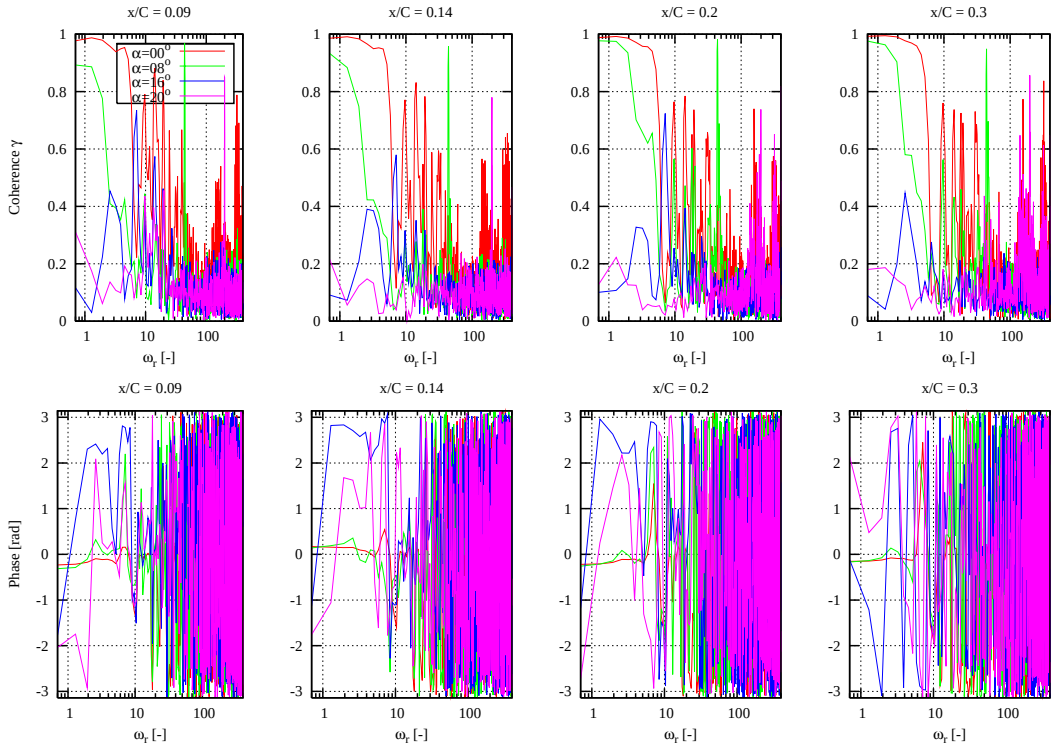

(b) Coherence and phase

Figure 16. Pressure Differences - No Turbulence Grid - x/C=0.09, 0.14, 0.2, 0.3

4.3 Pressure Difference

This section is dedicated to the analysis of the surface pressure characteristics related to the inflow turbulence. The surface pressure differences measured by the microphones are analyzed at several stations along the airfoil chord. The data analysis is identical to the previous section where the auto-spectra of the surface pressure differences between the suction and pressure sides are studied. However, in the present case, the analyzed data are obtained in the presence of turbulence grids in the wind tunnel located upstream of the airfoil section. Both the low and the high solidity grids are considered (see Section 2 for details on these grids). The latter grid should theoretically generate higher inflow turbulence intensity and/or smaller turbulence length scales, which will subsequently impinge on the airfoil section, than the former one. In addition, the same non-dimensionalized data are compared to the analytical model by Amiet [1, 2].

Experimental Data

For each grid, four angles of attack are chosen so that the corresponding flow conditions are similar to the four flow conditions studied in the previous section, namely: two cases at 0^o and 8^o angles of attack, both in the linear region; one case just after stall which corresponds to $\alpha = 19^o$ for the low solidity grid, and $\alpha = 20^o$ for the high solidity grid; and finally, one case for the fully stalled conditions which corresponds to $\alpha = 20^o$ for the low solidity grid, and $\alpha = 22^o$ for the high solidity grid.

The lift and drag characteristics as a function of the angle of attack effects are respectively displayed in Figs.17 and 21 for the low and the high solidity grid cases. The respective averaged pressure distributions on the airfoil are displayed on Figs.18 and 22.

Auto-spectra of the pressure differences along the airfoil chord are plotted in Figs.19(a) and 20(a) for the low solidity grid, and Figs.23(a) and 24(a) for the high solidity grid. Corresponding coherences and phase differences between the pressure on the suction and pressure sides are plotted in Figs.19(b) and 20(b) for the low solidity grid, and Figs.23(b) and 24(b) for the high solidity grid. Here, Figs.19 and 23 display the data for $x/C = 0.01$, 0.025, 0.04 and 0.06, whereas Figs.20 and 24 display the data for $x/C = 0.09$, 0.14, 0.2 and 0.3. These data are plotted as a function of the reduced frequency ω_r defined in the previous section.

Before starting the actual analysis of the results, it must be noted that the experimental data measured in the case of the low or the high solidity grid are very similar. Only very small differences can be observed and it can therefore be concluded that the inflow turbulence characteristics experienced by the airfoil section are very similar for the two turbulence grids (as it was already observed in Section 3). Hence, the following analysis does not differentiate the two cases, except if specifically mentioned in the text. The only noticeable difference between the two cases is the angle of attack at which stall does occur (see Figs.17 and 21). However, the difference is relatively quite small (of the order of only 1^o).

Analysis of Results Not Related to Inflow Turbulence

A series of patterns that were observed in the previous section (when no turbulence grid was present) can be recognized in the present cases. In a first place, the stall phenomenon is characterized by higher spectral energy in the low frequency range at all chordwise locations for the two stalled cases: $\alpha = 19^o$ and 20^o for the low solidity grid, and $\alpha = 20^o$ and 22^o for the high solidity grid.

Transition to turbulence of the boundary layer can also be observed at the chord locations $x/C = 0.14$ for $\alpha = 0^o$, and $x/C = 0.04$ for $\alpha = 8^o$. It is in both cases further

upstream on the airfoil surface than in the case without turbulence grid, which is expected since the presence of inflow turbulence must have a destabilizing effect on the laminar boundary layer and thereby trigger earlier transition to turbulence. The occurence of transition coincides with a sudden drop of the coherence between the pressure and suction side pressures as observed in the previous section. As for the two higher angles of attack (i.e. in stalled conditions), the transition to turbulence cannot clearly be observed on the auto-spectra. It can be surmised that it does occur further upstream the first reported chordwise position $x/C = 0.01$.

The separation of the flow on the suction side of the airfoil can also be observed in Figs.18 and 22 for the two higher angles of attack: at $x/C \approx 0.14$ for $\alpha = 19^o$ and $x/C \approx 0.06$ for $\alpha = 20^o$ with the low solidity grid, and at $x/C \approx 0.14$ for $\alpha = 20^o$ and at $x/C \approx 0.04$ for $\alpha = 22^o$ with the high solidity grid. However, the sudden appearance of an energy peak that was observed in the cases without turbulence grid cannot clearly be observed here. Indeed, even if the same phenomenon does occur in the present cases, its effect might be somehow blurred by the presence of the inflow turbulence, which might contaminate the spectra and overlap with the present phenomenon.

Analysis of Results Related to Inflow Turbulence

As concluded above, the location of transition to turbulence of the laminar boundary layer is significantly modified by the presence of the inflow turbulence, due to its destabilizing effect. In addition, the occurence of stall is also influenced by the presence of the grid. It is now focused on effects which specifically originate from inflow turbulence.

A quite interesting feature specific to the inflow turbulence can be observed on the phase plots in Figs.19(b) and 23(b) for low angles of attack ($\alpha = 0^o$ and 8^o), and for chordwise locations near the trailing edge ($x/C = 0.01$ and to a lesser extent at $x/C = 0.025$). In the frequency range $2 < \omega_r < 20$ to 30, so-called anti-phasing of the surface pressure difference fluctuations can be observed. It is characterized by phase differences close to $+\pi$ or $-\pi$ together with relatively high coherence levels. This phenomenon does occur when inflow turbulent vortices of relatively high length scales compare to the airfoil thickness impinge on the airfoil. In such cases, inflow turbulent vortices can be idealized as a sinusoidal wave with oscillating lower and higher pressures. The low and high pressure regions present in a vortex split between the upper and lower sides of the airfoil. It results in turbulent pressure fluctuations on both sides of the airfoil that are out of phase.

Comparison with Amiet's Model

The next part of the analysis is concerned with a comparison of the previous results with the analytical theory developped by Amiet [1, 2] (see Mish and Devenport [18] for details about the implementation of the model used in this work, which is also reported in Appendix C). In these references, an analytical model based on an assumed isotropic incoming turbulence together with the theory of inviscid flow over a flat plate without mean loading is devised. This results in a model which only requires as input parameters the inflow turbulence intensity I and the turbulence integral length scale Λ. These parameters will be deduced from the study of the inflow turbulence chararacteristics performed in Section 3.1. Arbitrary values will also be used in order to fit the model results to the measurements.

Influence of Turbulence Intensity

Three values of the turbulence intensity are tested: $I = 1.5, 0.8$ and 0.4%. The first value corresponds approximately to the value observed in the LM wind tunnel for the high solidity grid at the corresponding wind speed (see Section 3.1,

Fig.5(c)). In the three cases, the turbulence integral length scale is set to $\Lambda = 0.015\,\mathrm{m}$ as approximately evaluated in Section 3.1.

Amiet's model results are compared to experimental ones only for the measurements performed with the high solidity grid at $\alpha = 0^o$ in Fig.25(a). It can be seen that Amiet's model predicts quite well the experimental auto-spectra in the case $I = 0.4\%$ near the trailing edge ($x/C \leq 0.04$), but largely overestimates the measured results for the actual turbulence intensity $I = 1.5\%$. A possible explanation for this fact is a possible rapid turbulence intensity decay from the hot-wire device location to the airfoil location as it is convected downstream. Therefore, the airfoil might experience a lower turbulence intensity than the hot-wire. The calculated turbulence intensity might as well for some reason have been overestimated in Section 3.1.

Further downstream on the airfoil surface, the pressure fluctuations calculated by Amiet's model decay more rapidly than the experimental ones. It is possible that the airfoil surface turbulent boundary layer plays a role in this process and intensifies the turbulent pressure fluctuations.

Nevertheless, it can be seen that the slope of the experimental spectra for reduced frequencies in the range $15 < \omega_r < 100$ is very well predicted by the model for all turbulence intensities. For higher frequencies ($\omega_r > 100$), the microphone measurements are known to be disturbed by resonance effects in the microphone cavity (as clearly illustrated by the high energy peak in the end of the spectra).

It should be noted here that some misinterpretations of the results could originate from the dimensionalization of the model formulation which is not clearly defined (in the author's opinion), and from the definition of the error and Fresnel functions in the references [20]. Some further inquiries have to be conducted in order to clarify these points.

Influence of Integral Length Scale

The next study concerns the influence of the turbulence integral length scale Λ in Amiet's model. Three different test values are chosen: $\Lambda = 0.015, 0.005$ and $0.001\,\mathrm{m}$. The first value corresponds to the integral length scale measured in the wind tunnel with the high solidity grid (see Section 3.1, Fig.6(c)). The turbulence intensity is set to $I = 1.5\%$. The results are displayed in Fig.25(b), together with the present experimental results obtained with the high solidity grid at an angle of attack $\alpha = 0^o$. As it can be observed, the experimental value $\Lambda = 0.015\,\mathrm{m}$ reasonably predicts the frequency locations of the auto-spectrum maximum values. However, a better auto-spectrum level is predicted near the trailing edge ($x/C = 0.01$) for the value $\Lambda = 0.05\,\mathrm{m}$ indicating that the calculated integral length scale might have been somehow overestimated in Section 3.1.

Influence of Angle of Attack

The last analysis is concerned with identical auto-spectra for the pressure differences, but this time the spectra are non-dimensionalized by the inflow dynamic pressure $q = 0.5\rho U_\infty^2$. The results are presented at 6 different chordwise locations in Fig.26(a). In each of these figures, the following angles of attack are considered: $\alpha = 0$, 4, 8, 12, 16 and 20^o. In addition, the results obtained with Amiet's model are reported ($I = 1.5\%$ and $\Lambda = 0.015\,\mathrm{m}$), but the conclusions to be drawn from the model results are the same as above. Indeed, it can be observed that Amiet's model overpredicts the experimental results for $\alpha = 0^o$, but that the slope of the spectra is well predicted.

An interesting result is the decrease of the slope of the experimental spectra in the frequency range $7 < \omega_r < 100$ as the angle of attack increases. This phenomenon was also observed by Mish and Devenport [18]. However, in this article this resulted

in a decrease of the spectral energy at lower frequencies (where the spectra present a flat plateau) as the angle of attack increases. This was an original and striking results. It may be argued that the present experimental data do not reproduce this phenomenon because of very different turbulent conditions between the two experimental set-ups.

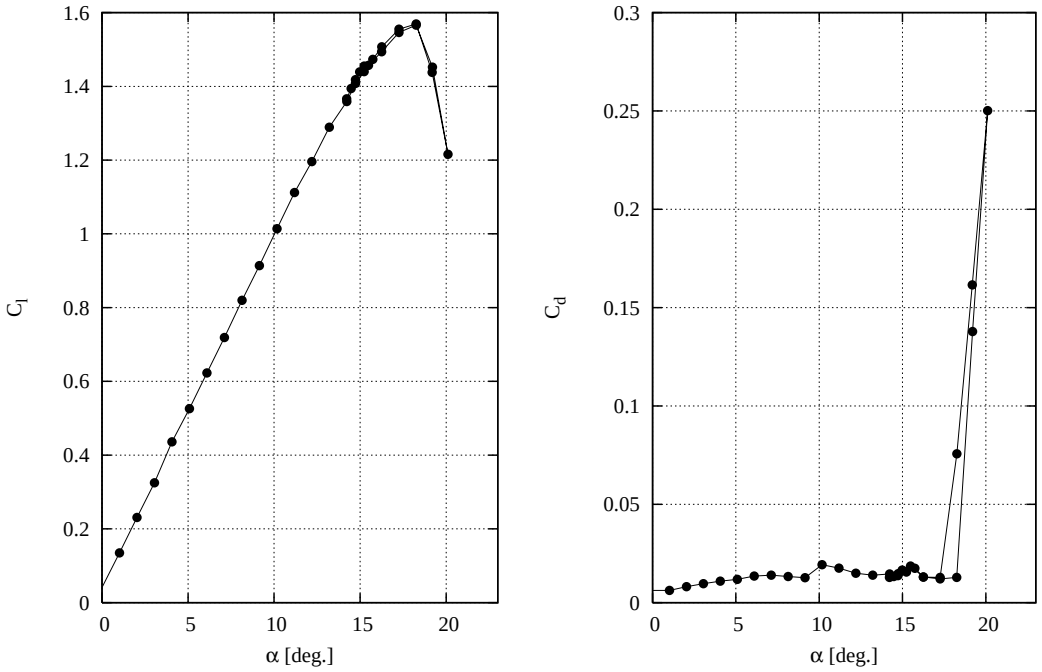

(a) Lift Coefficient (b) Drag Coefficient

Figure 17. Polar Characteristics - Low Grid Solidity

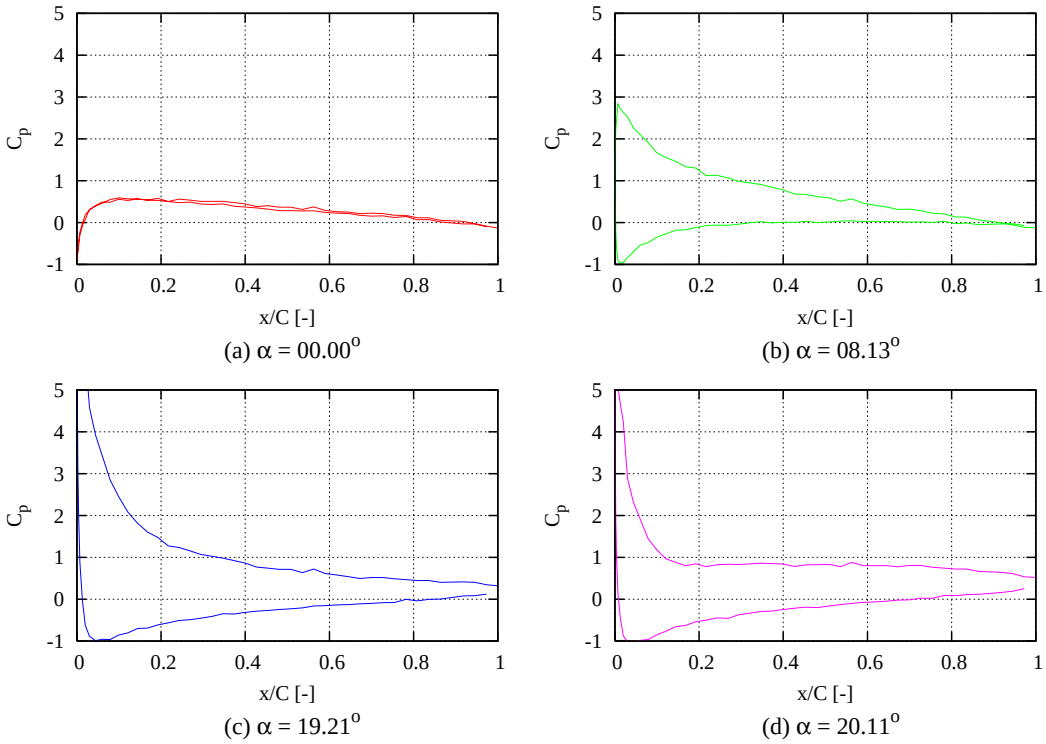

(a) α = 00.00° (b) α = 08.13°

(c) α = 19.21° (d) α = 20.11°

Figure 18. Pressure Coefficient Distributions - Low Grid Solidity

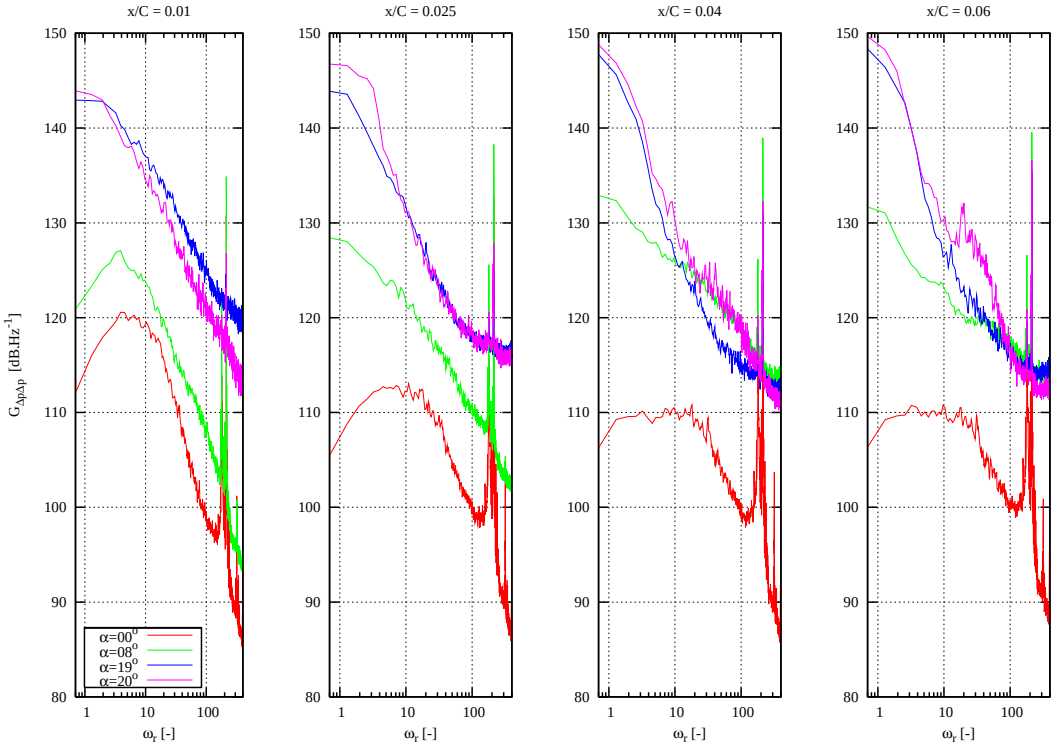

(a) Auto-spectrum of pressure difference

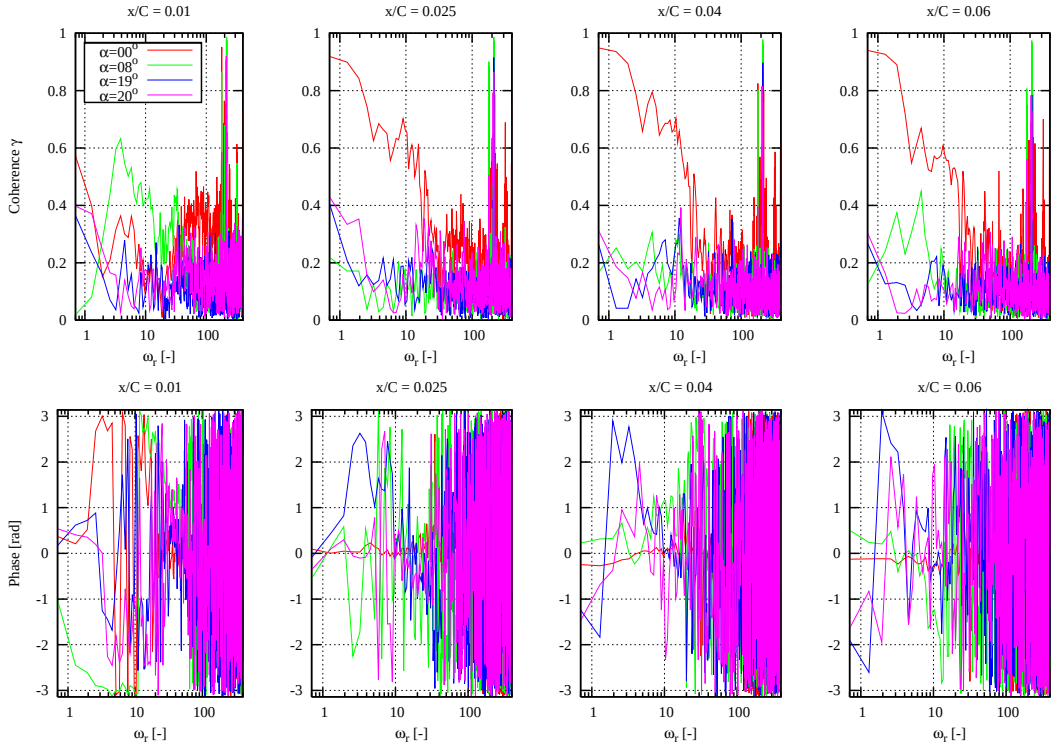

(b) Coherence and phase

Figure 19. Pressure Differences - Low Grid Solidity - x/C=0.01, 0.025, 0.04, 0.06

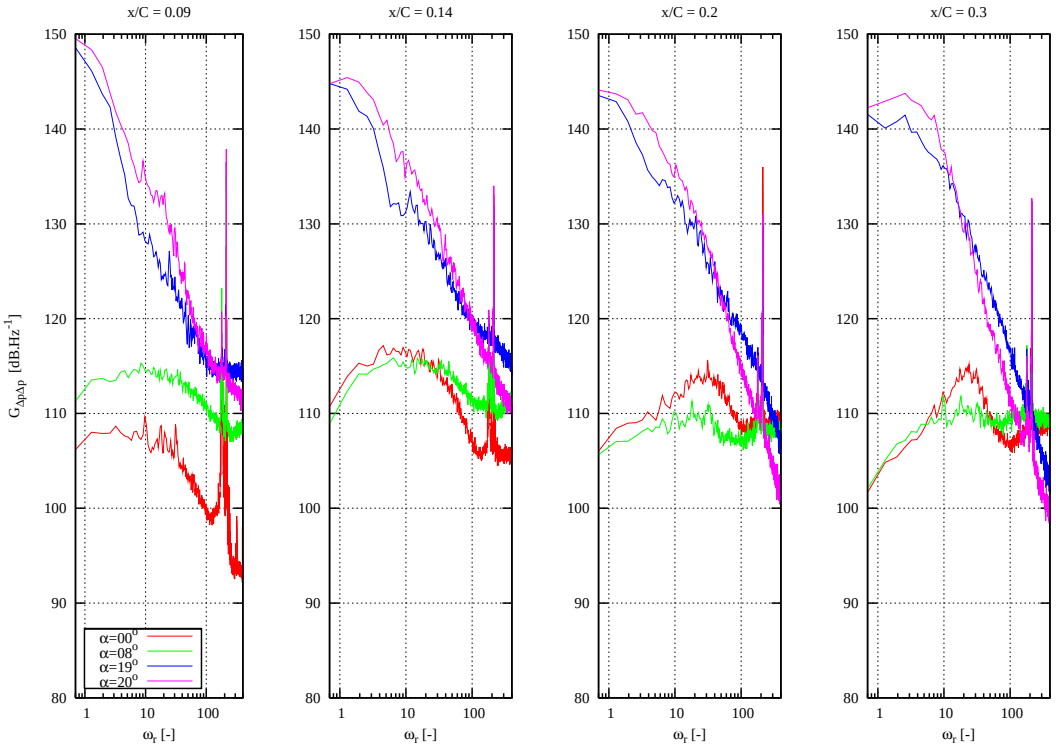

(a) Auto-spectrum of pressure difference

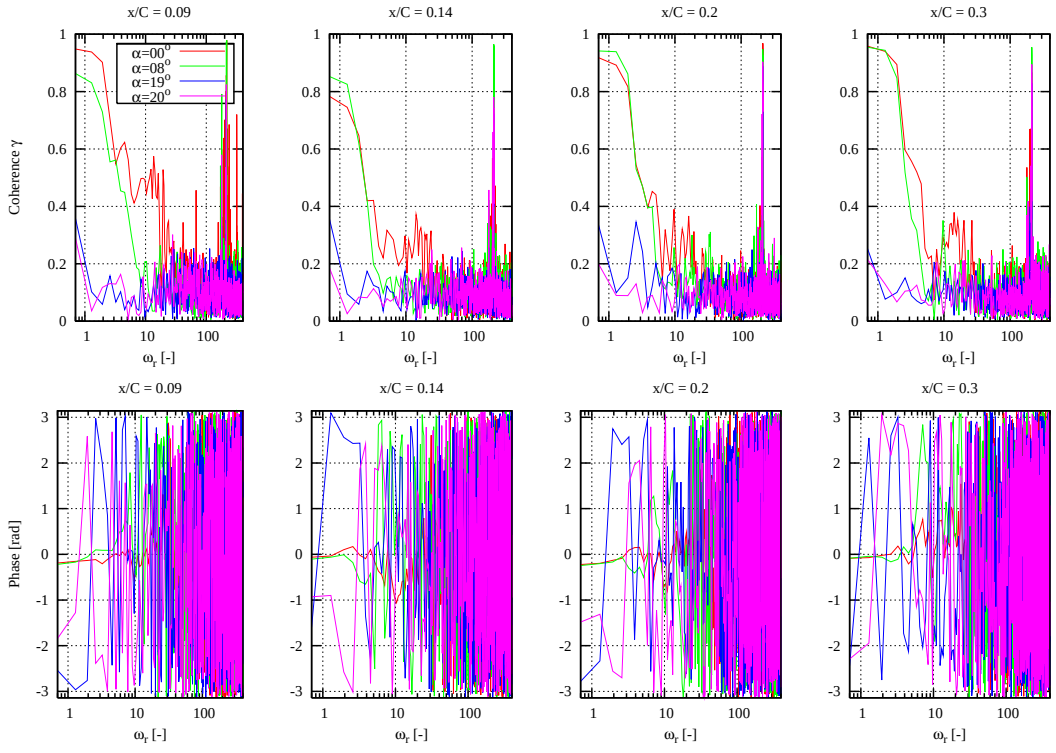

(b) Coherence and phase

Figure 20. Pressure Differences - Low Grid Solidity - x/C=0.09, 0.14, 0.2, 0.3

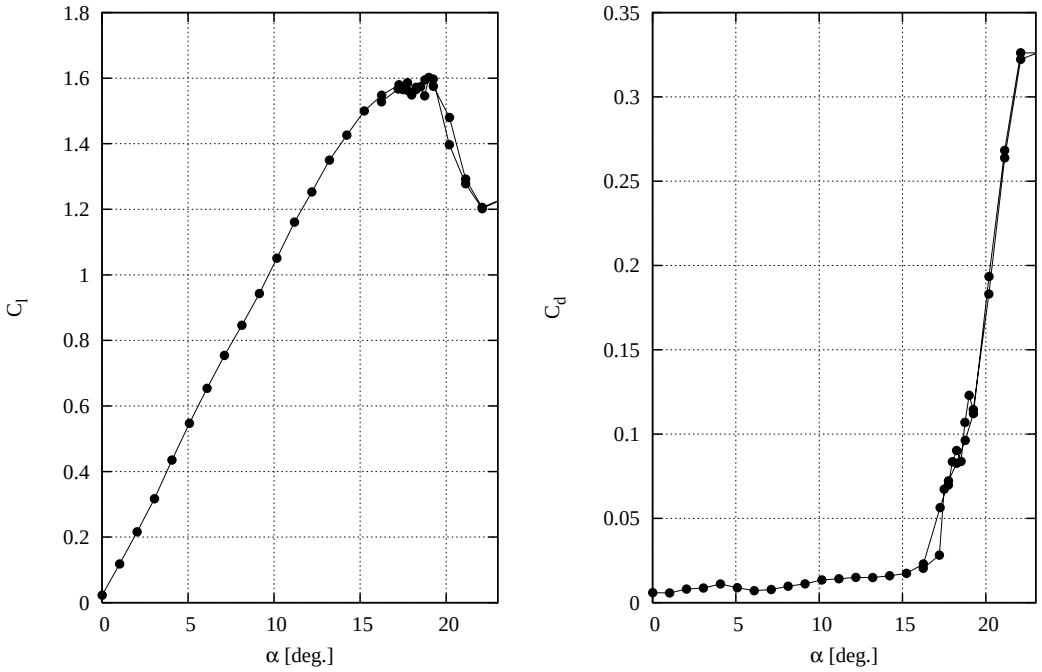

(a) Lift Coefficient (b) Drag Coefficient

Figure 21. Polar Characteristics - High Grid Solidity

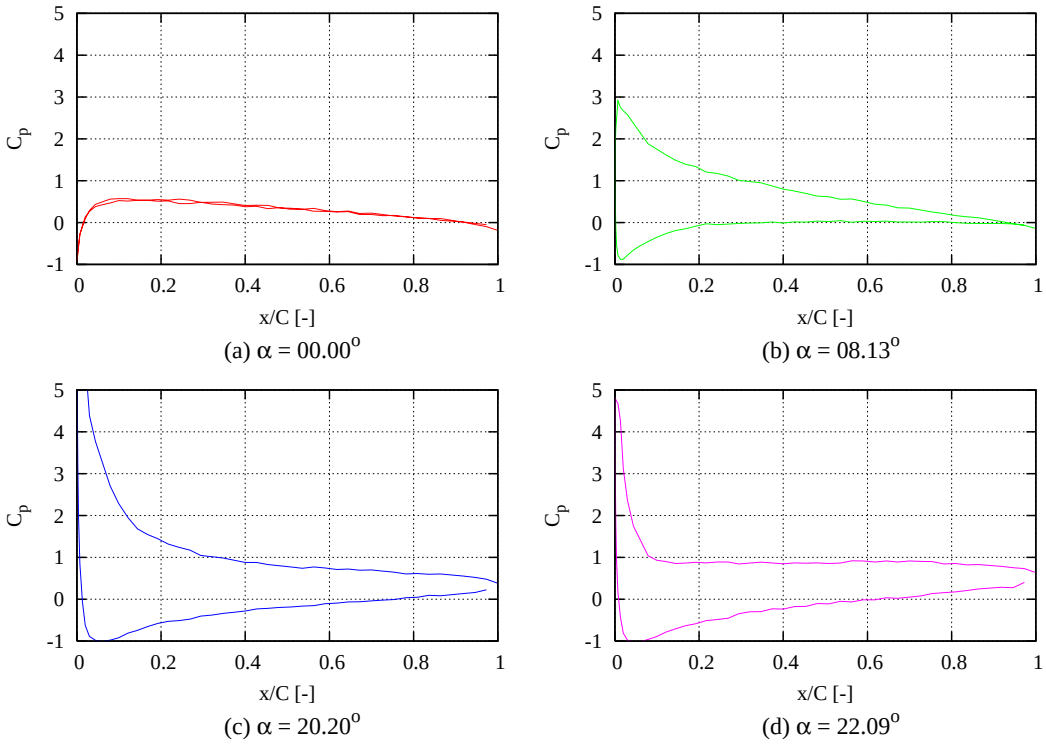

(a) α = 00.00° (b) α = 08.13°

(c) α = 20.20° (d) α = 22.09°

Figure 22. Pressure Coefficient Distributions - High Grid Solidity

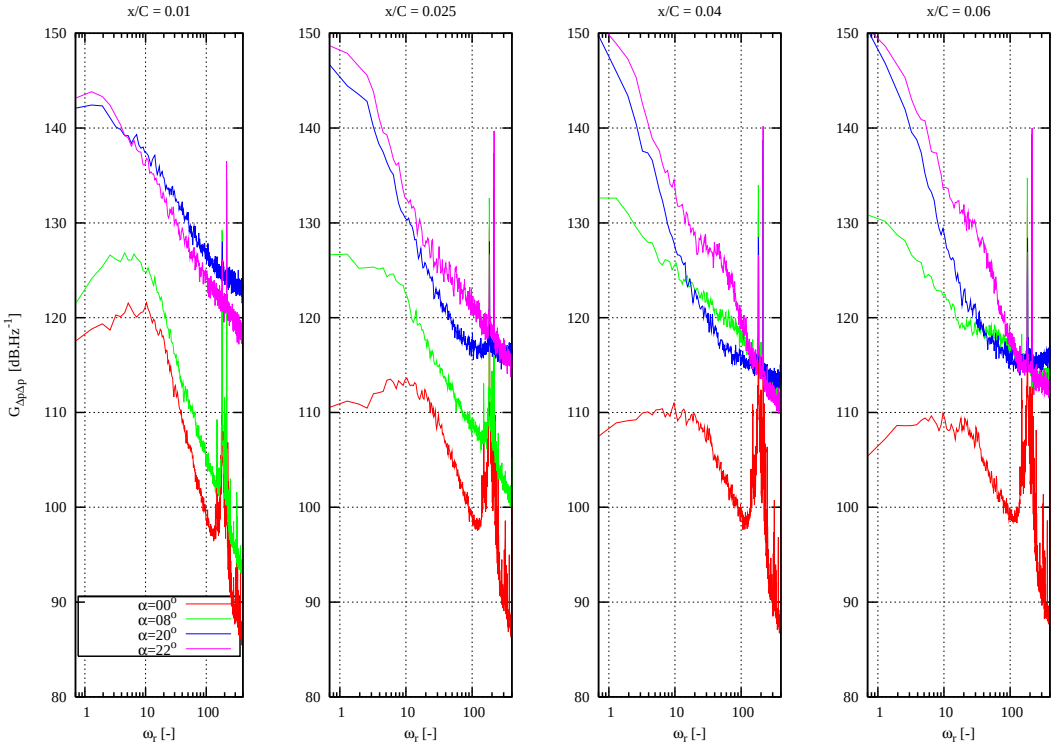

(a) Auto-spectrum of pressure difference

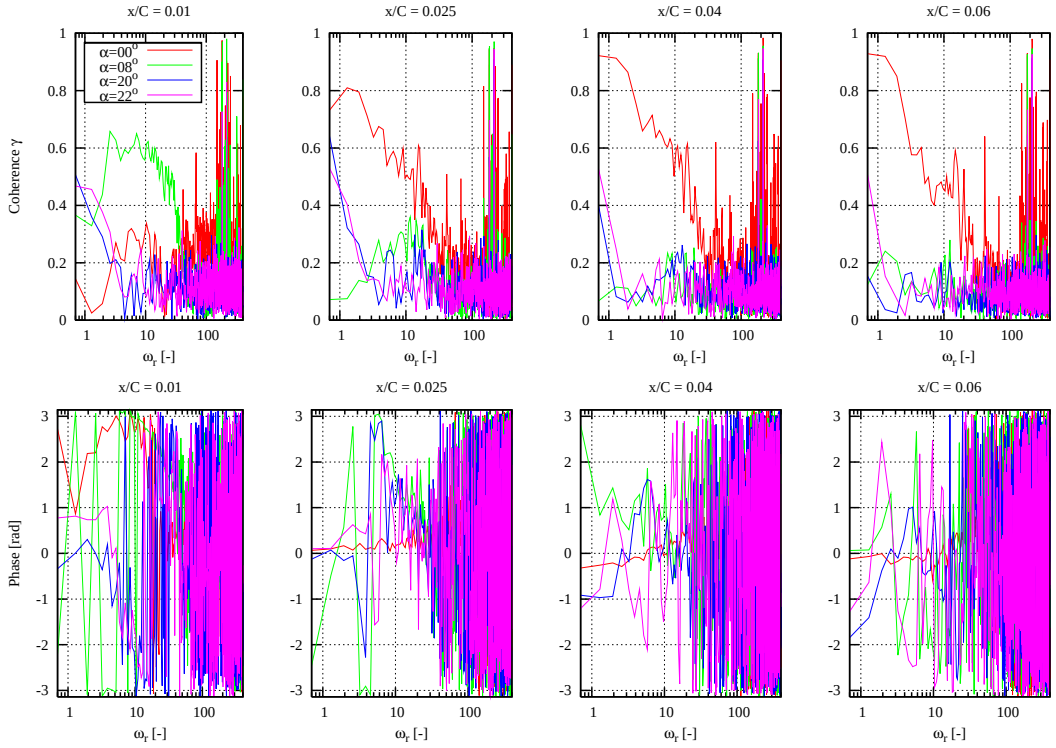

(b) Coherence and phase

Figure 23. Pressure Differences - High Grid Solidity - x/C=0.01, 0.025, 0.04, 0.06

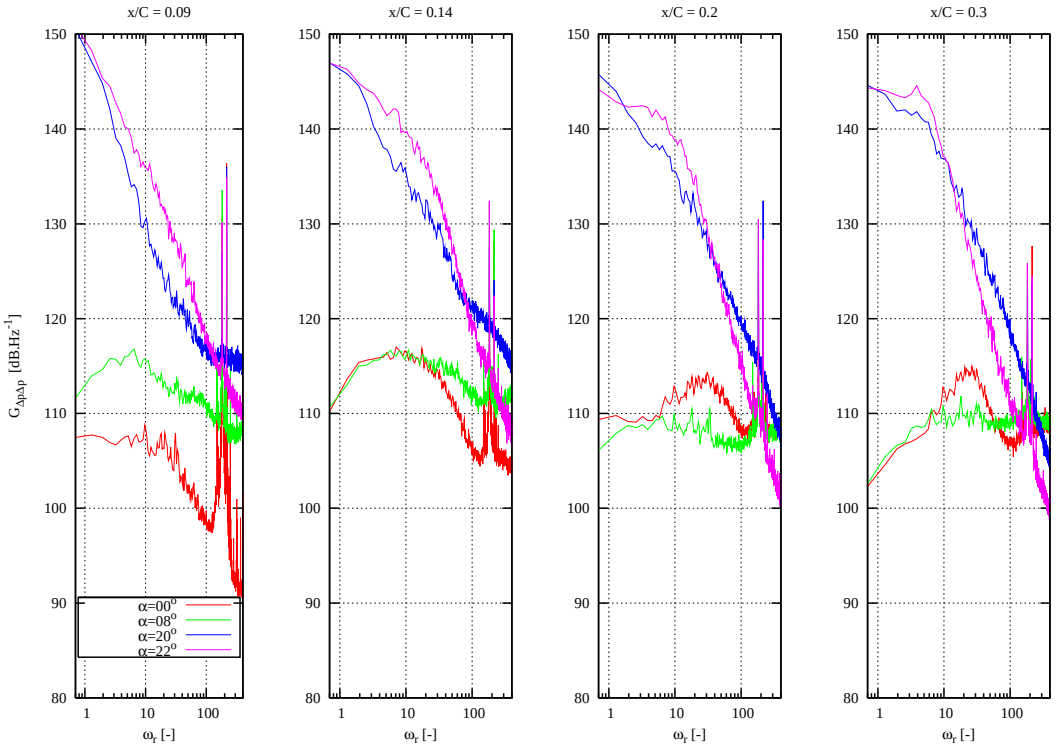

(a) Auto-spectrum of pressure difference

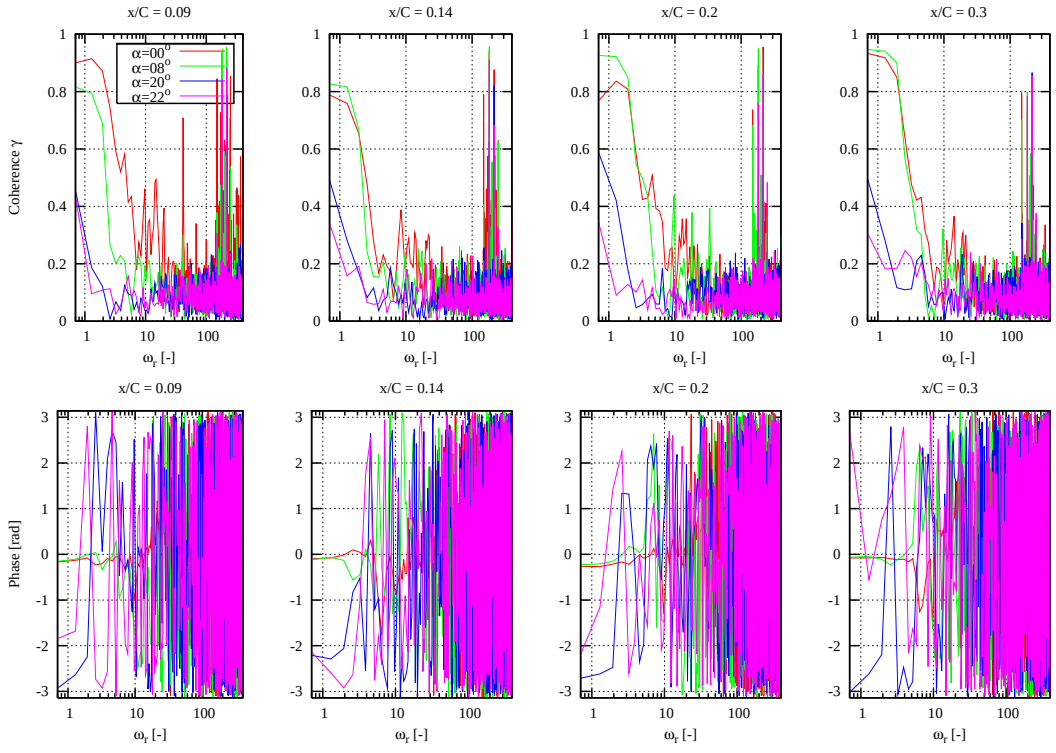

(b) Coherence and phase

Figure 24. Pressure Differences - High Grid Solidity - x/C=0.09, 0.14, 0.2, 0.3

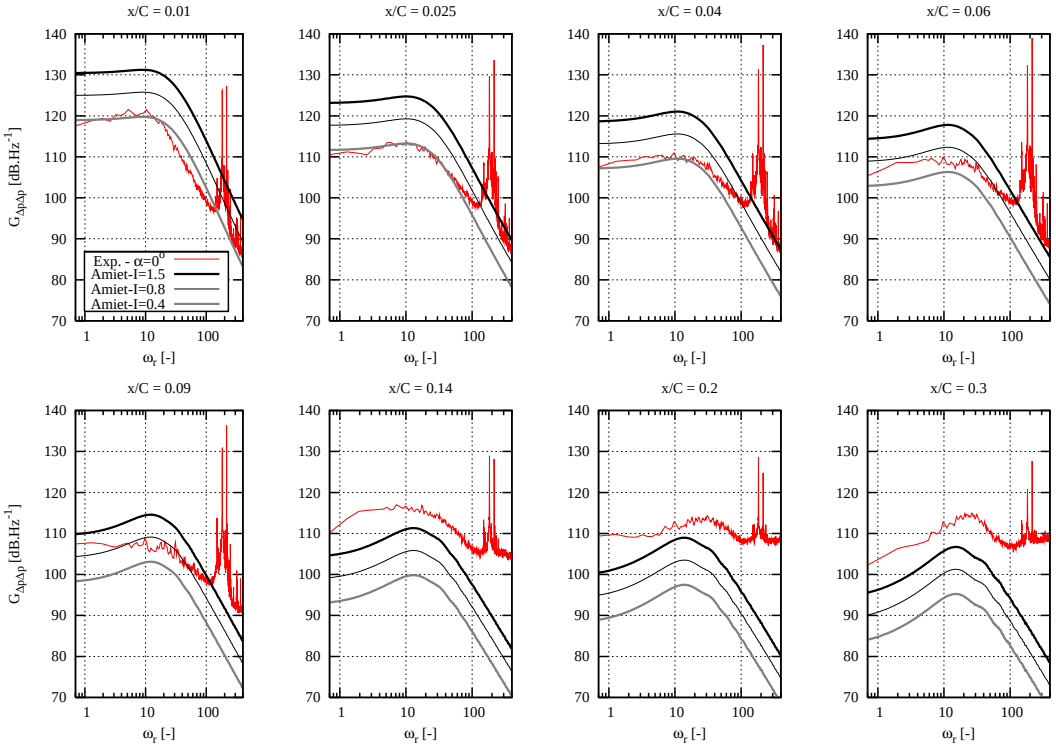

(a) Influence of turbulence intensity ($\Lambda = 0.015$ m)

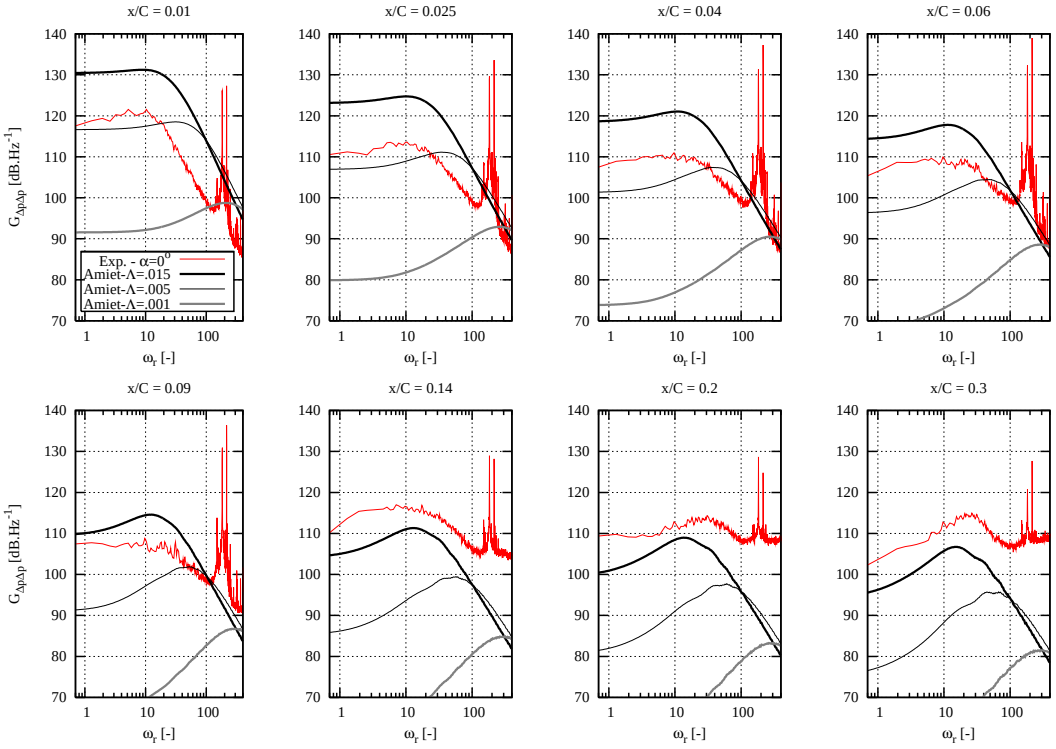

(b) Influence of integral length scale ($I = 1.5\%$)

Figure 25. Influence of Input Parameters in Amiet's Model - High Grid Solidity

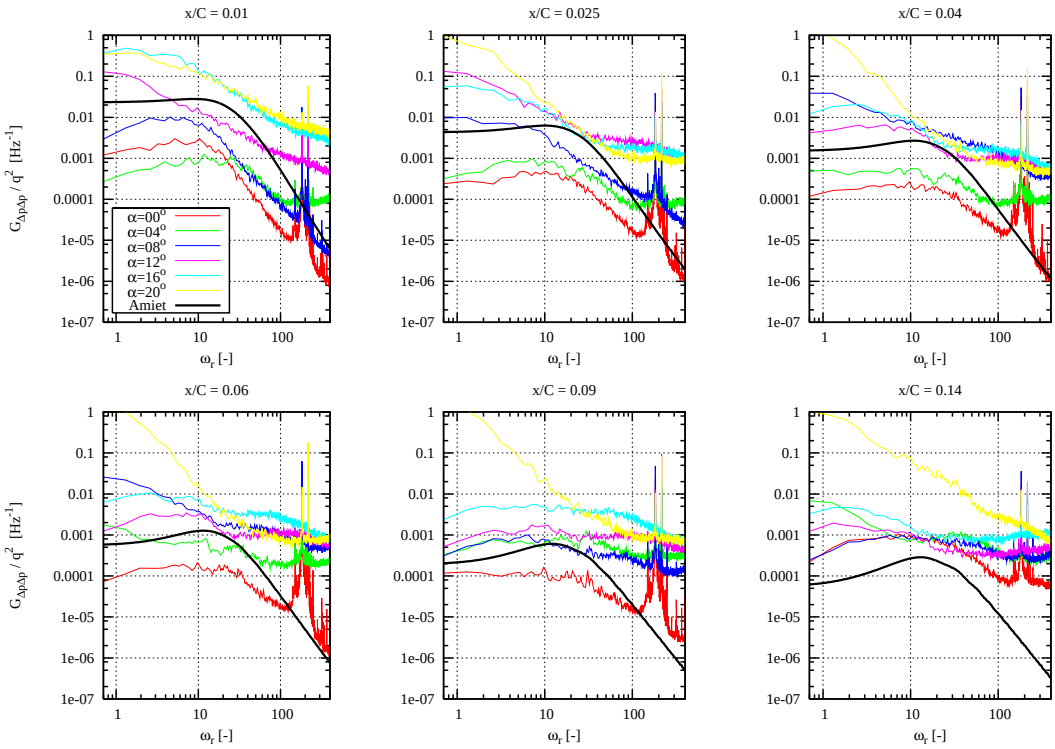

Figure 26. Influence of Angle of Attack - High Grid Solidity

4.4 Spatial Coherence

In this section, the spatial coherence of the turbulent pressure fluctuation differences (between the pressure and suction sides of the airfoil) are studied both in the chordwise direction at a given spanwise location, and spanwise at a given chordwise location.

4.4.a Chordwise Coherence

Definitions

The chordwise coherence function as a function of chordwise location x proposed by Mish [20] reads:

$$\gamma_{\text{Mish}}(x) = \frac{|G_{\Delta P \Delta P'}|}{G_{\Delta P \Delta P}}$$

where the cross-spectral density of pressure differences at two different chordwise stations is defined as:

$$G_{\Delta P \Delta P'} = G_{P_1 P_1'} + G_{P_2 P_2'} - 2 \cdot G_{P_1 P_2'}$$

$G_{PP'}$ is the cross-spectral density of the pressure fluctuations at points P and P'. Here, the prime ($'$) is used to denote the chordwise station $x'/C = 0.01$, whereas unprimed quantities denote other chordwise stations. The subscripts 1 and 2 denote the suction and the pressure sides, respectively.

However, the classical way of defining the coherence, which is used in the present work, reads:

$$\gamma(x) = \frac{|G_{\Delta P \Delta P'}|}{\sqrt{G_{\Delta P \Delta P} \cdot G_{\Delta P' \Delta P'}}}$$

where the cross-spectral density between two different chordwise stations is given as:

$$G_{\Delta P \Delta P'} = G_{P_1 P_1'} + G_{P_2 P_2'} - G_{P_1 P_2'} - G_{P_1' P_2}$$

The coherence according to Amiet's model can then be defined by using the cross-spectrum given in Appendix C and the following formula:

$$\gamma_{\text{Amiet}}(x, f) = \frac{|S_{\Delta P \Delta P'}(\overline{x}, \overline{x'}, 0, f)|}{\sqrt{S_{\Delta P \Delta P}(\overline{x}, \overline{x}, 0, f) \cdot S_{\Delta P' \Delta P'}(\overline{x'}, \overline{x'}, 0, f)}}$$

where the non-dimensionalized chordwise abscisse is defined as $\overline{x} = 2x/C$.

Experimental Data

The pressure difference coherence between the chordwise station $x'/C = 0.01$ and other stations further downstream the airfoil at the same spanwise location are plotted as a function of the chordwise coordinates in logarithmic scale in Fig.27. Each subfigure displays the results for different normalized reduced frequencies. In the first raw, the considered reduced frequencies are: $\omega_r = 1.123$, 2.928, 5.836 and 11.648, which are more characteristic of large scale turbulence flow features. The second raw displays the data for the following reduced frequencies: $\omega_r = 3.056$, 6.112, 31.515 and 58.783, which are more relevant for small scale turbulence. The previous values were chosen in accordance with those chosen by Mish [20]. Results for three angles of attack $\alpha = 0$, 2 and 8^o are only reported here, together with the results corresponding to the analytical model by Amiet [1, 2] as discussed in the previous section. Data originating from the measurements performed with the high solidity turbulence grid are reported only. No significant difference was found with the low solidity grid results.

Analysis of Results

As far as the experimental results for $\alpha = 0^o$ are concerned, a peculiar behaviour of the coherence can be observed at nearly all frequencies. Indeed, after an initial decay of the coherence as the chordwise abscisse increases ($x/C \leq 0.04$), the coherence presents a new increasing phase (in the region to $0.04 < x/C < 0.09$) reaching non-negligeable values. Thereafter, the coherence returns to smaller values. This behaviour was also observed when using the coherence definition proposed by Mish.

The influence of the input parameters for Amiet's model is also studied. It is found that the turbulent intensity has no influence on the coherence. Indeed, the turbulence intensity only modifies the amplitude of the pressure response spectrum, and is therefore removed when the coherence is computed. However, the turbulence integral length scale does influence the results as it can be observed in Fig.27. The results obtained with $\Lambda = 0.001\,\mathrm{m}$ somehow better match the experimental results at an angle of attack $\alpha = 0^o$ than with $\Lambda = 0.015\,\mathrm{m}$. This is in contrast with the comparison performed with the normalized pressure difference auto-spectra in Section 4.3, where an opposite tendency was observed.

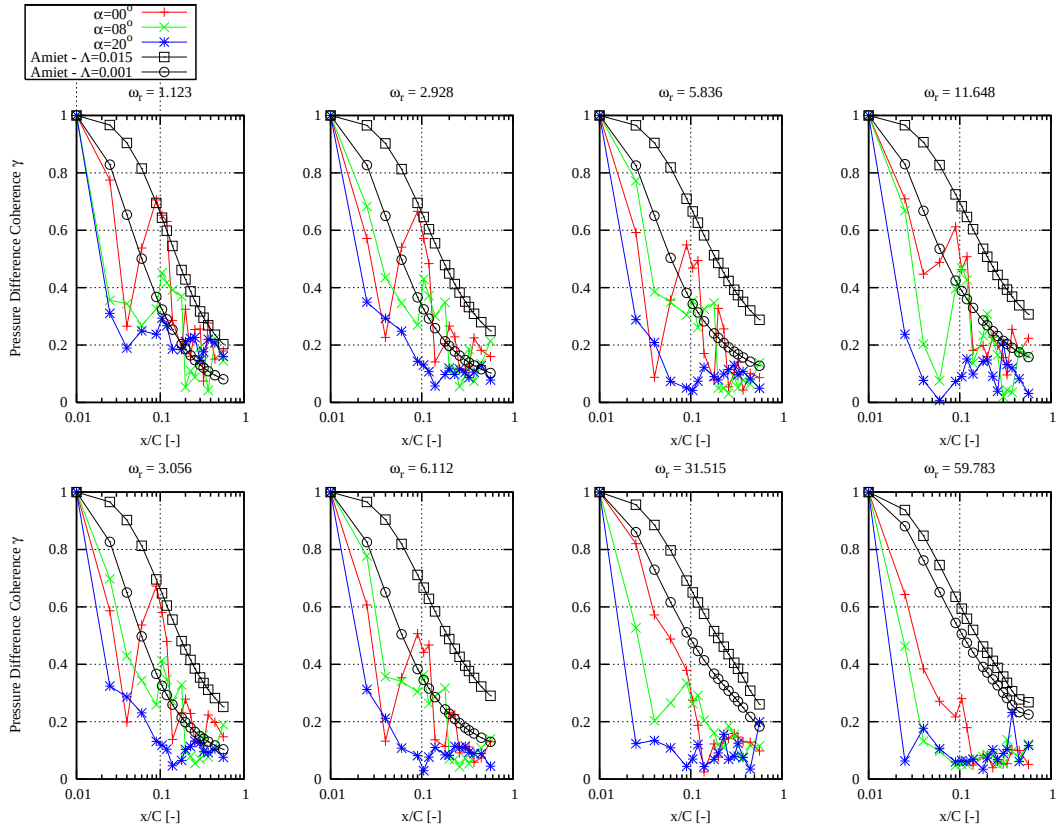

Figure 27. Pressure Differences Chordwise Coherence - High Grid Solidity

4.4.b Spanwise Coherence

Definitions

The spanwise coherence function as a function of spanwise separation length Δz proposed by Mish [20] reads:

$$\gamma_{\text{Mish}}(\Delta z) = \sqrt{\frac{|G_{\Delta P \Delta P'}|^2}{G_{\Delta P \Delta P} \cdot G_{\Delta P' \Delta P'}}}$$

where the cross-spectral density of pressure differences at two different spanwise stations is defined as:

$$G_{\Delta P \Delta P'} = G_{P_1 P_1'} + G_{P_2 P_2'} - 2 \cdot G_{P_1 P_2'}$$

$G_{PP'}$ is the cross-spectral density of the pressure fluctuations at points P and P'. Here, the prime ($'$) is used to denote the spanwise station $z'/C = 0.33$, whereas unprimed quantities denote other spanwise stations. The subscripts 1 and 2 denote the suction and the pressure sides, respectively.

The classical way of defining the coherence is detailed in the previous Section 4.4.a and is used in the present work.

The coherence according to Amiet's model can be defined by using the cross-spectrum given in Appendix C and the following formula:

$$\gamma_{\text{Amiet}}(x, \Delta z, f) = \frac{|S_{\Delta P \Delta P'}(\overline{x}, \overline{x}, \overline{\Delta z}, f)|}{|S_{\Delta P \Delta P}(\overline{x}, \overline{x}, 0, f)|}$$

where $\overline{x} = 2x/C$ is the non-dimensionalized chordwise abscisse, and the spanwise separation length Δz is similarly non-dimensionalized.

Experimental Data

The pressure difference coherence between the spanwise station $z'/C = 0.33$ and other stations on the airfoil at the same chordwise location are plotted as a function of the spanwise separation in Fig.28(a) for $x/C = 0.025$, and Fig.28(b) for $x/C = 0.09$. Each subfigure displays the results for different normalized reduced frequencies (see previous section for details). Results for three angles of attack $\alpha = 0$, 2 and 8^o are reported, together with the results corresponding to the analytical model by Amiet [1, 2] as defined above. Two values of the turbulent integral length scale are tested: $\Lambda = 0.015$ and 0.001 m. Data originating from the measurements performed with the high solidity turbulence grid are reported only. No significant difference was found with the low solidity grid results.

Analysis of Results

Similarly to the chordwise coherence, the results are not influenced by the turbulence intensity used as input in Amiet's model. As it can be observed on Fig.28(a-b), the model results are rather slightly influenced by the turbulence integral length scale. At low frequency and near the trailing edge ($x/C = 0.025$), there is a good quantitative agreement between the experimental and the model results. This deteriorates significantly for higher frequencies ($\omega_r \geq 31.515$), and further downstream on the airfoil ($x/C = 0.09$).

Note that the peculiar behaviour (for which the coherence presents after its initial decay an increasing phase before returning to small values) observed with the chordwise coherence is also observed here. However, in the case $x/C = 0.025$, the phenomenon is concentrated to small values of the spanwise separation length.

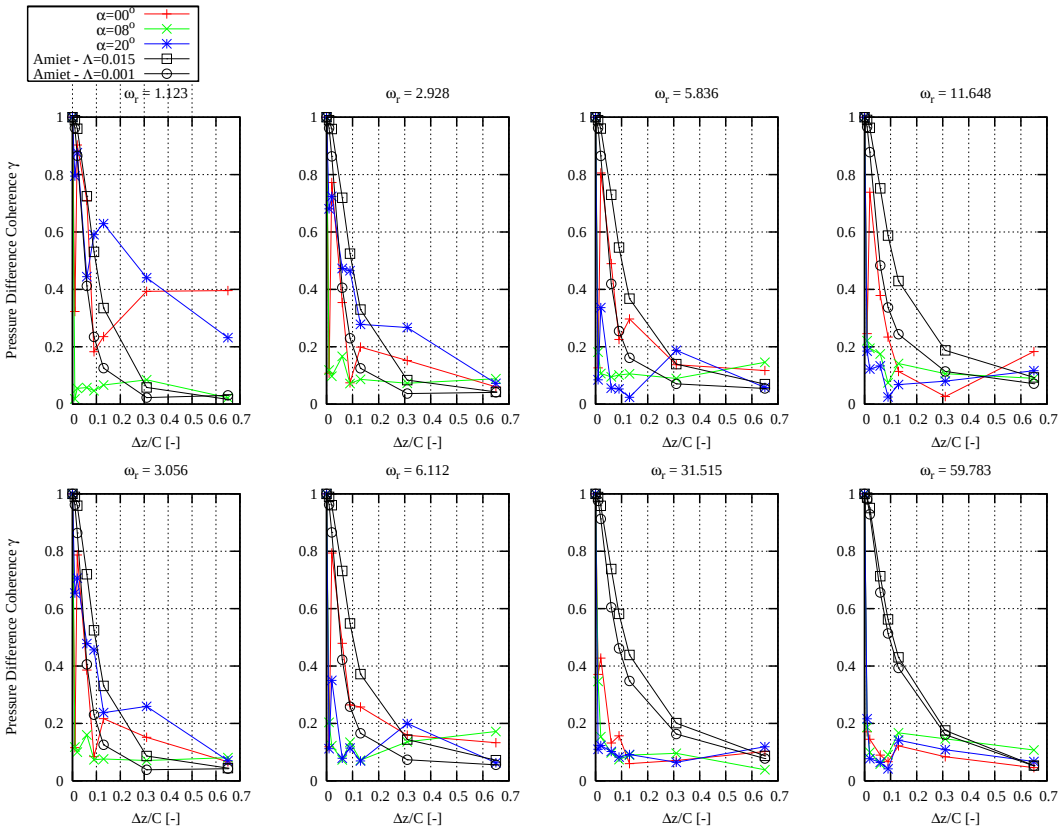

(a) x/C=0.025

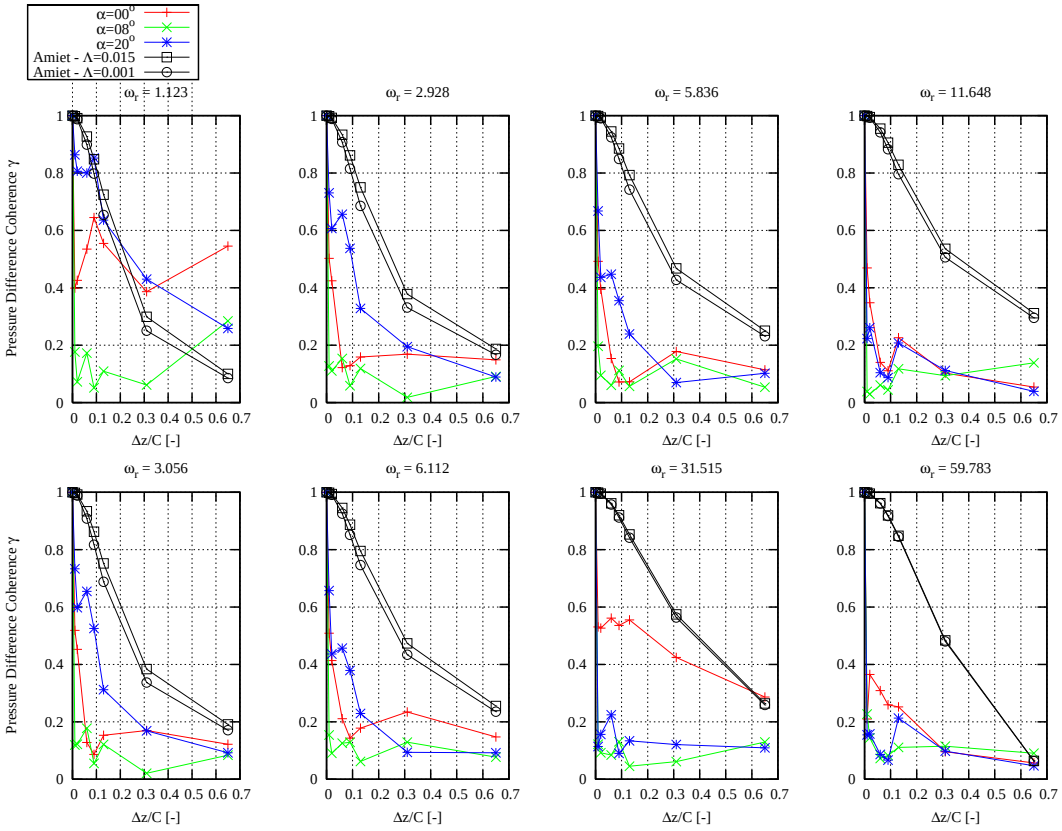

(b) x/C=0.09

Figure 28. Pressure Differences Spanwise Coherence - High Grid Solidity

5 Trailing Edge Noise

The aim of this section is the study of the airfoil surface microphone measurements in the perspective of trailing edge noise. The part of the model that is used for this study is discussed and results are compared with measurements data.

5.1 TNO Model and Surface Pressure Fluctuations

As far as the TNO trailing edge noise model is concerned (see Appendix D for a detailed description of the model) and before expressing the noise generated in the far field, this model is based on the knowledge of the boundary layer turbulence characteristics near the trailing edge and the resulting description of the surface pressure fluctuations. The wavenumber-frequency surface pressure spectrum $\Phi_p(\boldsymbol{k},\omega)$ is given in Eq.(D.12) in Appendix D. The frequency surface pressure spectrum, which is also accessible from the microphone measurements, can then be calculated by integrating over the entire wavenumber space as:

$$\Phi_p(\omega) = \iint_{-\infty}^{+\infty} \Phi_p(\boldsymbol{k},\omega)\,\mathrm{d}k_1\mathrm{d}k_3 \tag{1}$$

where $\boldsymbol{k} = (k_1, 0, k_3)$. It is reminded here that the TNO model described in Appendix D is only valid if the boundary layer flow is turbulent (i.e. if the transition from laminar to turbulent flow has already occured upstream along the airfoil surface) and if the flow is attached. Therefore, the model validity can be compromised at low angles of attack and low Reynolds numbers when the flow remains laminar over the airfoil, or at higher angles of attack when the flow over the airfoil suction side is detached. The boundary layer data are obtained with the in-house Navier-Stokes solver EllipSys2D (see references for details [16, 17, 24]).

5.2 Analysis of Surface Pressure

The experimental spectrum at several stations along the airfoil chord are displayed in Figs.29, 30 and 31 for inflow velocities corresponding to Reynolds numbers based on the airfoil chord equal to $Re = 1.6, 3$ and 6×10^6, respectively. Only the cases with the no turbulence grid are considered here. On these figures, the measurement data plotted with fine lines for four angles of attack $\alpha = 0, 4, 8$ and 12^o are compared with the TNO model results plotted with thick lines. As it can be seen, the model predicts the increase of spectral energy of the surface pressure fluctuations as the angle of attack increase. The spectral levels are rather well predicted in the high frequency range $f > 1000\,\mathrm{Hz}$, in particular towards the trailing edge ($x/C = 0.567$) and for the highest Reynolds number. However, there exist large errors in the spectral levels predicted at lower frequencies.

Note that some of the model results at lower angles of attack largely overpredict model results at higher angles of attacks near the trailing edge (see Fig.29 for $x/C \leq 0.45$, Fig.30 or Fig.31 for $x/C \leq 0.33$). This is due to the fact that transition has not yet occured in these cases at these locations and the model is however used even if not valid for laminar flows.

Fig.32 presents similar results for various Reynolds numbers at $x/C = 0.567$ and for an angle of attack $\alpha = 0^o$. The influence of the presence of turbulence grids on the measured data can be observed. As expected from the study in the previous sections, only very small differences can be observed between the high and low solidity grids. The measured spectra are slightly higher for the case without grid at $Re = 1.6 \times 10^6$, but this can be attributed to the fact that the transition

location is located slightly upstream thereby energizing the boundary layer at the microphone location. Conclusions concerning the TNO model results are similar to those drawn above.

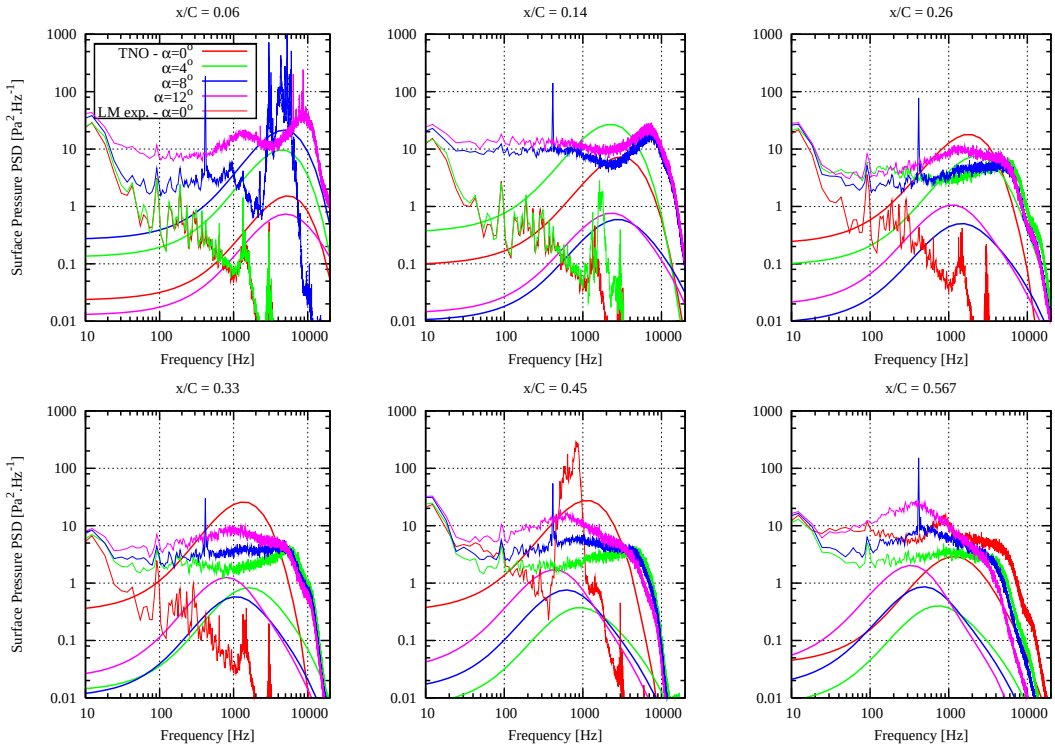

Figure 29. Surface Pressure Spectra along Airfoil Chord - $Re = 1.6 \times 10^6$

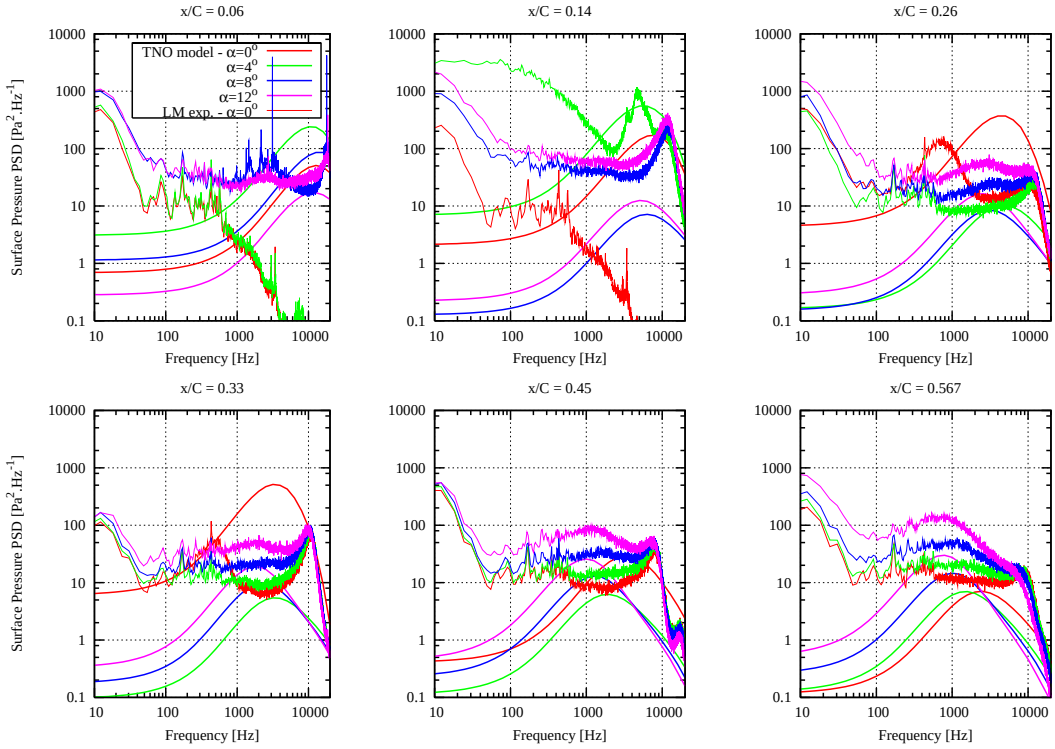

Figure 30. Surface Pressure Spectra along Airfoil Chord - $Re = 3 \times 10^6$

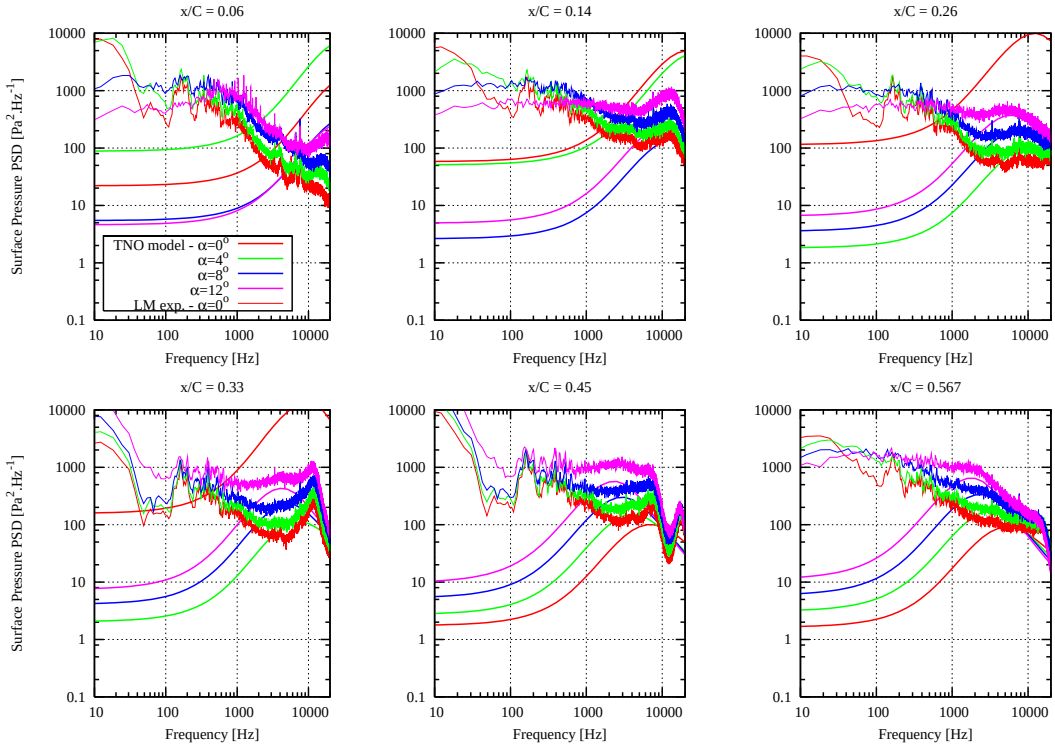

Figure 31. Surface Pressure Spectra along Airfoil Chord - $Re = 6 \times 10^6$

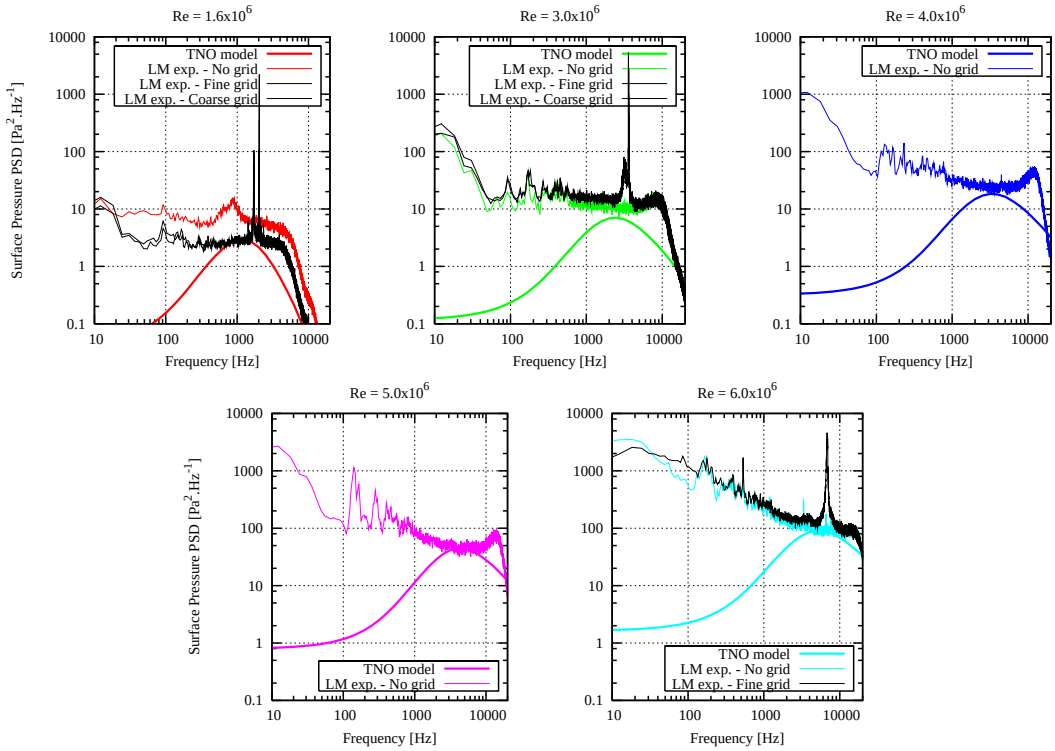

Figure 32. Surface Pressure Spectra at $x/C = 0.567$ - $\alpha = 0^o$

6 Conclusions

In this report, an analysis of the LM Glasfiber wind tunnel measurements performed with high-frequency microphones placed on the NACA0015 airfoil surface was conducted. It provided some relevant knowledge about the experimental conditions in the wind tunnel, as well as how to interpret the measured data. The turbulence characteristics in the wind tunnel were also investigated using hot-wire measurements.

In particular, it was observed several times during this study that both the low and high solidity turbulence grids generate incoming flows onto the airfoil section that have very similar turbulence characteristics. In comparison to the results obtained by Mish and Devenport [18], it seems that a thicker frame for the turbulence grids would produce more comparable results, or at least generate larger turbulence length scales in the flow. Indeed, a thicker frame would provide an increased surface facing the incoming laminar flow, which would in turn generate larger vortical structures as required to match more closely the above-mentioned results.

When analyzing and comparing the measurements with the turbulent inflow noise model by Amiet [1, 2], substantial differences were observed even if the model input parameters characterizing the turbulence properties were deduced from hot-wire measurements in the wind tunnel. As for the analysis of measurements in the perspective of trailing edge noise according to the TNO model by Parchen [22], the comparisons showed large discrepancies in particular in the low frequency range. However, in both cases some of the features and tendencies of the acoustic phenomena of interest were captured by the models.

In addition, there is a need to clarify a few points concerning the dimensionalization choices, as well as the definition of the error function used in Amiet's model as derived by Mish [20].

Acknowledgements

This work was carried out under a contract with the Danish Technical Research Council (STVF), Prediction and Reduction of Noise from Wind Turbines, 2004-2007. Part of the work presented in this report was also sponsored by the Danish Energy Authorities within the Energy Research Project "Program for Research in Applied Aeroelasticity, EFP-2007". We are very thankful to LM Glasfiber for allowing access to their wind tunnel facility.

References

[1] Amiet, R.K., "Airfoil Response to an Incompressible Skewed Gust of Small Spanwise Wave-Number", AIAA J., Vol.14, No.4, pp.541-542, 1976.

[2] Amiet, R.K., "High-Frequency Thin Airfoil Theory for Subsonic Flow", AIAA J., Vol.14, No.8, pp.1076-1082, 1976.

[3] Batchelor, G.K., The Theory of Homogeneous Turbulence, Cambridge University Press, Cambridge, U.K., 1953.

[4] Blake, W.K., Mechanics of Flow-Induced Sound and Vibration, Vol.I and II, in Applied Mathematics and Mechanics, Frenkiel, F.N. and Temple, G. (eds.), Academic Press, 1986.

[5] Brooks, T.F., and Hodgson, T.H., "Trailind Edge Noise Prediction from Measured Surface Pressures", J. Sound Vib., Vol.78, No.1, pp.69-117, 1981.

[6] Champagne, F.H., Friehe, C.A., LaRue, J.C., and Wyngaard, J.C., "Flux Measurements, Flux Estimation Techniques, and Finescale Turbulence Measurements in the Unstable Surface Layer over Land", J. Atmos. Sci., Vol.34, pp.515-530, 1977.

[7] Champagne, F.H., "The Finescale Structure of the Turbulent Velocity Field", J. Fluid Mech., Vol.86, pp.67-108, 1978.

[8] Chase, D.M., "Noise Radiated from an Edge in Turbulent Flow", AIAA J., Vol.13, No.8, pp.1041-1047, 1975.

[9] Drela, M., "XFOIL: An Analysis and Design System for Low Reynolds Number Airfoils", in Low Reynolds Number Aerodynamics, Mueller, T.J. (ed.), Lecture Notes in Engineering, Vol. 54, Springer-Verlag, Berlin, pp.1-12, 1989.

[10] Døssing, M., "High Frequency Microphone Measurements for Transition Detection on Airfoils", Tech. Rep. Risø-R-1645(EN), Risø-DTU, Roskilde, Denmark, 2008.

[11] Hinze, J.O., *Turbulence*, McGraw Hill, 1959.

[12] Jørgensen, F.E., How to Measure Turbulence with Hot-Wire Anemometer - A Practical Guide, Dantec Dynamics, A/S, 2002. Available at:http://www.dantecdynamics.com/Admin/Public/

[13] Lumley, J.L., Stochastic Tools in Turbulence, Academic Press, 1970.

[14] Lutz, T., Herrig, A., Würz, W., Kamruzzaman, and Krämer, E., "Design and Wind-Tunnel Verification of Low-Noise Airfoils for Wind Turbines", AIAA Journal, Vol.45, No.4, pp.779-785, 2007.

[15] Mathieu, J., and Scott, J., Introduction to Turbulent Flow, Cambridge University Press, Cambridge, U.K., 2000.

[16] Michelsen, J.A., "Basis3D - A Platform for Development of Multiblock PDE Solvers", Tech. Rep. AFM 92-05, Technical University of Denmark, 1992.

[17] Michelsen, J.A., "Block Structured Multigrid Solution of 2D and 3D Elliptic PDE's", Tech. Rep. AFM 94-06, Technical University of Denmark, 1994.

[18] Mish, P.F., and Devenport, W.J., "An Experimental Investigation of Unsteady Surface Pressure on an Airfoil in Turbulence – Part 1: Effects of Mean Loading", J. Sound Vib., Vol.296, pp.417-446, 2006.

[19] Mish, P.F., and Devenport, W.J., "An Experimental Investigation of Unsteady Surface Pressure on an Airfoil in Turbulence – Part 2: Sources and Prediction of Mean Loading Effects", J. Sound Vib., Vol.296, pp.447-460, 2006.

[20] Mish, P.F., "An Experimental Investigation of Unsteady Surface Pressure on Single and Multiple Airfoils", Ph.D. Dissertation, Aerospace and Ocean Engineering Department, Virginia Tech., March 2003. Available at: http://scholar.lib.vt.edu/theses/available/etd-03312003-173021/

[21] Papenfuß, H.D., Aerodynamic Commissioning of the New Wind Tunnel at LM Glasfiber A/S (Lunderskov), Private Communication, Institut für Thermo- und Fluiddynamik, Ruhr-Universität Bochum, Bochum, June 2006.

[22] Parchen, R., "Progress report DRAW: A Prediction Scheme for Trailing-Edge Noise Based on Detailed Boundary-Layer Characteristics", TNO Rept. HAG-RPT-980023, TNO Institute of Applied Physics, The Netherlands, 1998.

[23] Press, W.H., Teukolsky, S.A., Vetterling, W.T., and Flannery, B.P., Numerical Recipes in Fortran 77: The Art of Scientific Computing (Second Edition), Cambridge University Press, 1992.

[24] Sørensen, N.N., "General Purpose Flow Solver Applied to Flow over Hills", PhD Thesis, Tech. Rep. Risø-R-827-(EN), Risø National Laboratory, Roskilde, Denmark, June 1995.

[25] Schlichting, H., *Boundary Layer Theory*, McGraw Hill, 1968.

[26] Tennekes, H, and Lumley, J.L., A First Course in Turbulence, The MIT Press, 1972.

[27] Wagner, S., Guidati, G., and Ostertag, J., "Numerical Simulation of the Aerodynamics and Acoustics of Horizontal Axis Wind Turbines", Proc. of the 4^{th} European Comp. Fluid Dyn. Conf., Athens, Papailiou, K. (ed.), Vol.2, pp.436-441, 1998.

A Hot-Wire Measurements

A.1 Hot-Wire Calibration

Tri-axial sensor probes designed for the measurements of three-dimensional turbulent velocity fields were purchased from Dantec Dynamics (see the user guide for details about the probes and their calibration [12]). Although a software designed for the calibration and analysis of the raw measurements data was also provided, a preliminary study in the Velux wind tunnel showed that the final results were corrupted in some way. It is therefore decided here to implement this calibration analysis within an in-house Fortran code.

As mentioned in Section 2, the temperature in the wind tunnel can be kept approximately constant. As a consequence, the calibration related to temperature variations is omitted and can be considered as being implicitly included in the following velocity calibration coefficients.

Hot-wire measurements for each of the three sensors provide a voltage E (in Volts) that can be related to a calibrated inflow velocity U_{cal} (in m/s) through the following 4^{th} order polynomial approximation:

$$U_{cal} = C_0 + C_1 \cdot E + C_2 \cdot E^2 + C_3 \cdot E^3 + C_4 \cdot E^4$$

where the C_i's are calibration constants to be defined. In our case, these are calculated by using a procedure from Numerical Recipes (see [23], Section 3.5, subroutine 'polcof'). In order to define these constants, five different reference wind speeds have to be considered. Note that the resulting calibration polynomial should not be used outside of this velocity range as it may oscillate. The measured signals from the sensors E are averaged over time for each of the five runs. The resulting values are related to their respective averaged velocity in the wind tunnel U_{cal}, which is independently measured by a pitot tube located elsewhere in the wind tunnel.

The previous analysis is performed for the each of the three probe sensors and results in three sets of calibration constants, yielding in turn three calibration velocities $\{U_{cal1}, U_{cal2}, U_{cal3}\}$. The wind speed velocities in the wire-coordinates system $\{U_1, U_2, U_3\}$ are then calculated by inverting the following 3×3 matrix:

$$\begin{aligned}
k_1^2 \cdot U_1^2 + \quad U_2^2 + h_1^2 \cdot U_3^2 &= (1 + k_1^2 + h_1^2) \cdot \cos^2(35.3^o) \cdot U_{cal1}^2 \\
h_2^2 \cdot U_1^2 + k_2^2 \cdot U_2^2 + \quad U_3^2 &= (1 + k_2^2 + h_2^2) \cdot \cos^2(35.3^o) \cdot U_{cal2}^2 \\
U_1^2 + h_3^2 \cdot U_2^2 + k_3^2 \cdot U_3^2 &= (1 + k_3^2 + h_3^2) \cdot \cos^2(35.3^o) \cdot U_{cal3}^2
\end{aligned}$$

Note that there is a typing error in the formula given in the user guide report provided by Dantec Dynamics [12], p.31. In the present experiment, fiber-film sensors were prefered to gold-plated wire sensors for solidity reasons. The conductivity-related coefficients provided by the manufacturer are:

$$k_i^2 = k^2 = 0.04 \quad \text{and} \quad h_i^2 = h^2 = 1.20 \qquad (i = 1, 2, 3)$$

Finally, the velocity components in the probe coordinate system (U, V, W) can be deduced from the previously calculated values as:

$$\begin{aligned}
U = &+\cos(54.74^o) \cdot U_1 + \cos(54.74^o) \cdot U_2 + \cos(54.74^o) \cdot U_3 \\
V = &-\cos(45.0^o) \cdot U_1 - \cos(135.0^o) \cdot U_2 + \cos(90.0^o) \cdot U_3 \\
W = &-\cos(114.09^o) \cdot U_1 - \cos(114.09^o) \cdot U_2 - \cos(35.26^o) \cdot U_3
\end{aligned}$$

These components are readily the velocity components in the wind tunnel coordinate system for which U corresponds to the streamwise direction (assuming the probe was aligned with the main flow direction when mounted in the wind tunnel).

A.2 Error Analysis

An error analysis of the measurement data is now performed. The classical theory of propagation of error is used. Namely, the uncertainty in any calculated function f of the experimentally measured quantities $\{x_i,\, i = 1, \ldots N\}$, with respective statistically independent uncertainties $\{\Delta x_i,\, i=1, \ldots N\}$, reads:

$$\Delta f = \pm \sqrt{\sum_{i=1}^{N} \Big(\frac{\partial f}{\partial x_i}\Big)^2 (\Delta x_i)^2}$$

In case the measured quantities are correlated in some way, their covariance matrix has to be introduced in the previous formula.

Firstly, it is arbitrarily assumed that the only experimental errors in the measurement set-up are the hot-wire voltage measurements E_1, E_2, E_3. These errors are assumed statistically independent, but with identical amplitudes ΔE. As examples, the cases with high solidity turbulence grid and without grid are considered. In both cases, the uncertainties are evaluated for two wind tunnel velocities: $U_\infty \approx 50$ and 100 m/s. The calibrations are performed with the data measured at the following five wind speeds: $U_\infty \approx 25,\ 50,\ 70,\ 80,\ 100$ m/s. The relative uncertainties in the calculated velocities $\{U, V, W\}$ relatively to the voltage relative errors are reported in Table 2. As it can be seen, these ratios are roughly twice as large for the transverse components compared to the streamwise component, but always remain within acceptable proportions. They are slighly increasing with the inflow velocity, but are rather independent of the introduction of a turbulence grid in the wind tunnel.

	No Grid		High Solidity Grid	
U_∞	50 m/s	100 m/s	50 m/s	100 m/s
$\frac{\Delta U}{U} / \frac{\Delta E}{E}$	3.65	3.04	3.50	3.08
$\frac{\Delta V}{V} / \frac{\Delta E}{E}$	7.14	6.35	6.74	6.47
$\frac{\Delta W}{W} / \frac{\Delta E}{E}$	8.02	6.33	7.75	6.40

Table 2. Calculated Velocities to Sensor Voltage Relative Error Ratios

An error analysis is also conducted to investigate the influence of the errors on the given sensivity coefficients k^2 and h^2 onto the calculated velocities. As these coefficients do not (or very slightly) change during an experiment, these errors will only influence the average calculated velocities $\bar{U}$, $\bar{V}$ and $\bar{W}$. The results are reported in Table 3. It can be seen that the relative influence of these errors is negligeable.

	No Grid		High Solidity Grid	
U_∞	50 m/s	100 m/s	50 m/s	100 m/s
$\frac{\Delta \bar{U}}{\bar{U}} / \frac{\Delta k^2}{k^2}$	8.10^{-6}	4.10^{-6}	9.10^{-6}	5.10^{-6}
$\frac{\Delta \bar{V}}{\bar{V}} / \frac{\Delta k^2}{k^2}$	2.10^{-4}	2.10^{-4}	8.10^{-4}	6.10^{-4}
$\frac{\Delta \bar{W}}{\bar{W}} / \frac{\Delta k^2}{k^2}$	7.10^{-4}	5.10^{-4}	2.10^{-5}	7.10^{-5}
$\frac{\Delta \bar{U}}{\bar{U}} / \frac{\Delta h^2}{h^2}$	2.10^{-5}	1.10^{-5}	3.10^{-5}	2.10^{-5}
$\frac{\Delta \bar{V}}{\bar{V}} / \frac{\Delta h^2}{h^2}$	1.10^{-2}	9.10^{-3}	1.10^{-3}	2.10^{-4}
$\frac{\Delta \bar{W}}{\bar{W}} / \frac{\Delta h^2}{h^2}$	3.10^{-3}	2.10^{-3}	1.10^{-2}	1.10^{-2}

Table 3. Calculated Velocities to Sensivity Coefficients Relative Error Ratios

B Wind Tunnel Turbulence

The measurements performed by the hot-wire device (see previous Section A) which is placed in the wind tunnel section upstream of the airfoil profile can be used to characterize the turbulence that impinges the airfoil. The numerical techniques used to calculate the integral length scales, turbulence intensity and dissipation are presented here.

Note that the subscripts x, y and z refer to the streamwise and the two transversal flow directions, respectively. The indices 1, 2 and 3 will be sometimes used instead.

B.1 Correlation and Integral Length Scale

An integral scale can be defined as a measure of the longest correlation distance between two points in the flow that are separated either by space or time. In the present experimental set-up, the hot-wire measurements are performed at a single point in space. However, assuming Taylor hypothesis of frozen turbulence, an integral *length* scale can be evaluated.

For a given velocity component u_i ($i = 1, 2$ or 3), the corresponding integral length scale is defined by:

$$\Lambda_i = \frac{1}{\sigma_i^2} \int_0^{+\infty} R_{ii}(r)\, \mathrm{d}r \tag{B.2}$$

The auto-correlation function is given as:

$$R_{ii}(r) = < u_i(\boldsymbol{x} + \boldsymbol{r}, t)\, u_i(\boldsymbol{x}, t) >$$

where r is the norm of the separation vector $\boldsymbol{r}$, $\boldsymbol{x}$ is an arbitrary space location, and the operator $< \cdot >$ denotes the ensemble average. Note that isotropy and stationarity were assumed here, such that the correlation tensor is a function of r only. The variance σ_i^2 is the mean square value of the velocity component u_i and is also given as:

$$\sigma_i^2 = R_{ii}(0)$$

In practice, the integral in Eq.(B.2) is evaluated on a finite interval $[0, r_0]$, where r_0 denotes the distance at which the correlation function first cancels. Indeed, integrating over the overall spatial domain yields numerical inaccuracies which corrupt the results. It should be noted that in the case of measured velocity time-series, the integration interval will necessarily be finite.

Using the Wiener-Khinchin theorem, the auto-correlation function can be defined as the Fourier transform of the velocity power spectrum as:

$$R_{ii}(r) = \frac{1}{2\pi} \int_{-\infty}^{+\infty} S_{ii}(k)\, \mathrm{e}^{\mathrm{i}kr} \mathrm{d}k$$

where k is the wavenumber and $S_{ii}(k)$ is the power spectral density of the velocity u_i. This power spectral density is obtained from the Fourier transform of the velocity time-series $\hat{u}_i$ as:

$$S_{ii}(k) = \hat{u}_i(\omega)\, \hat{u}_i{}^*(\omega)$$

where the upper star $*$ indicates the complex conjugation. In the previous formula, the angular frequency ω is related to the wavenumber as:

$$k = \omega / U_c$$

according to the Taylor hypothesis. The convective velocity U_c denotes the velocity at which turbulence is convected by the flow. In our case, the wind tunnel averaged streamwise velocity is used.

Note that an integral length scale Λ_{ij} based on two distinct velocity components u_i and u_j $(i \neq j)$ can also be defined. In this case, the auto-correlation function has to be replaced by the cross-correlation $R_{ij}(r)$, and the power spectral density by the cross-spectral density of the two components.

B.2 Isotropic Turbulent Flow and Integral Scale

Another option for defining the integral length scale is to assume that the turbulent flow is isotropic and fit the classical Von Karman energy spectrum to the measured velocity spectrum. In practice, so-called one-point spectra for the three velocity components are obtained from the measurements (with the hot-wire device in our case) instead of energy spectra. The Von Karman energy spectrum of turbulence has the following form:

$$E(k) = \alpha\, \epsilon^{2/3} L^{5/3} \frac{(Lk)^4}{(1+(Lk)^2)^{17/6}} \tag{B.3}$$

where $E(k)\,\mathrm{d}k$ is half the variance of the wind velocity fluctuations in the range $[k, k+\mathrm{d}k]$, ϵ is the viscous dissipation of turbulence kinetic energy, L is the so-called outer integral scale (that defines the transition between the energy and the inertial subranges), and the scalar k is the norm of the wavenumber vector $\boldsymbol{k} = \{k_i,\, i = 1,2,3\}$. Experimental measurements of atmospheric boundary layer turbulence suggest that the empirical constant α can be approximated by $\alpha \approx 1.7$. In some other cases [3] (and in this report), the value 1.4528 is used. Assuming that the energy-containing eddies break up at a time scale equal to their turn-over time, the dissipation can be approximated as:

$$\epsilon \approx \frac{u_0^3}{L} \tag{B.4}$$

where u_0 is the characteristic velocity of the large energy-containing eddies. It is related to the variance σ_{1c}^2 of one of the fluid flow velocity components as $\sigma_{1c}^2 = u_0^2 = \sigma^2/3$, where σ^2 stands for the total variance of the turbulent velocity assuming isotropy.

The one-point spectra for the velocity components, which are measured in practice, are defined as a function of the spectral tensor as:

$$F_1(k_1) = \iint_{-\infty}^{+\infty} \Phi_{11}(\boldsymbol{k})\,\mathrm{d}k_2\mathrm{d}k_3$$

for the u_1 streamwise velocity component, and:

$$F_i(k_1) = \iint_{-\infty}^{+\infty} \Phi_{ii}(\boldsymbol{k})\,\mathrm{d}k_2\mathrm{d}k_3 \qquad (i = 2,3)$$

for the two other components. The spectral tensor $\boldsymbol{\Phi}$ takes the following form for an isotropic incompressible turbulent flow:

$$\Phi_{ij}(\boldsymbol{k}) = \frac{E(k)}{4\pi k^4}(k^2\delta_{ij} - k_i k_j)$$

Using this expression, introducing the Von Karman spectrum defined in Eq.(B.3), and integrating over the wavenumber space (see for example Lumley [13] for more details) finally yields to the following expressions for the one-point spectra:

$$F_1(k_1) = \frac{9\,\alpha\,\sigma_{1c}^2}{55} \cdot L \cdot \frac{1}{\left(1+(Lk_1)^2\right)^{5/6}} \tag{B.5}$$

and:

$$F_2(k_1) = F_3(k_1) = \frac{3\,\alpha\,\sigma_{1c}^2}{110} \cdot L \cdot \frac{3+8(Lk_1)^2}{\left(1+(Lk_1)^2\right)^{11/6}} \tag{B.6}$$

These functions, pre-multiplied by k_1, reach their respective maximum at the following values:

$$k_1|_{\max(k_1 F_1)} \approx 1.2247/L \quad \text{and} \quad k_1|_{\max(k_1 F_{2,3})} \approx 1.7824/L$$

Having measured the one-point spectra with the hot-wire device placed in the wind tunnel (and pre-multiplied with the streamwise wavenumber k_1), their maximum value can be located yielding estimated numerical values for the outer length scale L using the relationships defined above. Note that it is here assumed that such a length scale can be independently defined for each of the three components components.

The outer integral scale L is simply related to the wavenumber of the energy-containing eddies k_e as:

$$L = 1/k_e$$

In addition, for isotropic turbulence, the integral length scale $\widetilde{\Lambda}$ can be related to the previous wavenumber as [15]:

$$\widetilde{\Lambda} \approx 0.7468/k_e \tag{B.7}$$

Combining the previous equations, three integral length scales are related to the respective wavenumbers defining the maximum of the pre-multiplied one-point spectra as:

$$\widetilde{\Lambda}_x \approx 0.9147/k_1|_{\max(k_1 F_1)} \qquad \text{and} \qquad \widetilde{\Lambda}_{y,z} \approx 1.3312/k_1|_{\max(k_1 F_{2,3})} \tag{B.8}$$

B.3 Turbulence Intensity

The turbulence intensity I_i (expressed in %) for each of the velocity components is defined as :

$$I_i = 100 \times \frac{\sqrt{\sigma_i^2}}{U_\infty} = 100 \times \frac{\sqrt{< u_i^2 >}}{U_\infty} \tag{B.9}$$

whereas the 'total' turbulence intensity I is:

$$I = 100 \times \frac{\sqrt{\frac{1}{3}\sigma^2}}{U_\infty} = 100 \times \frac{\sqrt{\frac{1}{3} < \sum_{i=1}^{3} u_i^2 >}}{U_\infty} \tag{B.10}$$

The ensemble average is in practice evaluated by standard averaging using the measured time-series.

As in the previous section, the velocity variance can be adjusted so that a measured spectrum fits a given energy spectrum (or in practice the one-point velocity spectrum) such as the Von Karman spectrum. In other words, σ_{1c}^2 is adjusted so that the measured one-point spectrum fits the following integral:

$$\int_0^{+\infty} F_1(k_1)\,\mathrm{d}k_1 = \int_0^{+\infty} \frac{9\,\alpha\,\sigma_{1c}^2}{55} \cdot L \cdot \frac{1}{\left(1 + (Lk_1)^2\right)^{5/6}}\,\mathrm{d}k_1$$

where the outer integral scale L actually disappears from the right hand side during integration. It can be analytically integrated (for example with the help of a software like Mathematica©). The variance of the streamwise velocity component is then approximated as:

$$\widetilde{\sigma}_x^2 \approx \frac{1}{0.3442\,\alpha} \int_0^{+\infty} F_1(k_1)\,\mathrm{d}k_1$$

Similarly, integrating the one-point velocity spectra of the transversal velocity components yields the following results for the variances of these components:

$$\widetilde{\sigma}_{y,z}^2 \approx \frac{1}{0.3442\,\alpha} \int_0^{+\infty} F_2(k_1)\,\mathrm{d}k_1$$

The corresponding turbulence intensities $\widetilde{I}, \widetilde{I}_{x,y,z}$ can finally be computed using Eqs.(B.9) and (B.10) above.

B.4 Turbulent Dissipation

According to Tennekes and Lumley [26], under the assumption of local isotropy the turbulent kinetic energy dissipation rate ϵ reduces (from its tensorial form) to a function of the velocity derivative as:

$$\epsilon = 15\nu\overline{\left(\frac{\partial u}{\partial x}\right)^2}$$

where ν is the kinematic viscosity ($\nu \approx 1.58 \times 10^{-5}\,\mathrm{m}^2/\mathrm{s}$ at standard atmospheric conditions), x is the streamwise direction and u is the velocity in that direction. In the previous formula, the overline denotes a time average. The spatial derivative can be expressed as a time derivative assuming Taylor hypothesis as:

$$\frac{\partial u}{\partial x} = \frac{1}{U_\infty}\frac{\partial u}{\partial t}$$

The so-called Kolmogorov length scale that characterizes the scale at which molecular dissipation takes place, thereby ending the energy cascade from the large turbulent scales to the small ones, is related to the dissipation as:

$$\eta_K = \left(\frac{\nu^3}{\epsilon}\right)^{1/4}$$

Using the above equations, the time-series of the streamwise velocity component gives access to a first estimation of the Komogorov length scale.

Alternatively, using the value of the integral length scale $\widetilde{\Lambda}_x$ that was obtained by fitting the measured pre-multiplied one-point spectrum of the streamwise velocity component, and assuming that the turbulent dissipation can be related to the integral scale and the characteristic velocity of the energy-containing eddies according to equation (B.4), then a second Kolmogorov length scale can be estimated as:

$$\widetilde{\eta}_K = \left(\frac{\widetilde{\Lambda}_x}{0.7468}\right)^{1/4}\left(\frac{\nu}{\widetilde{\sigma}_x}\right)^{3/4}$$

where the approximation (B.7) has also been used.

To conclude this section, an approximation of the turbulent dissipation as a function of the measured velocity auto-spectrum is given. In the inertial subrange, dimensional analysis and isotropy lead to the -5/3 law of the velocity spectral decay as expressed by Eq.B.5. The one-point spectrum for the streamwise component can be rewritten as:

$$F_1(k_1) = \alpha_1 \epsilon^{2/3} k_1^{-5/3}$$

where ϵ is the dissipation rate of turbulence, and the univeral Kolmogorov constant α_1 should be close to 0.54. As described by Champagne *et al* [6], the dissipation rate within the inertial subrange is then given as:

$$\epsilon = \frac{2\pi}{U_\infty}\left(\frac{f^{5/3} S_u(f)}{\alpha_1}\right)^{3/2} \tag{B.11}$$

where f is the frequency, and $S_u(f)$ is the frequency auto-spectral density of the streamwise component in the inertial subrange. If the turbulent flow which is studied is characterized by a real isotropic inertial subrange, then the dissipation rate calculated as above should remain approximately constant within this frequency subrange.

C Amiet's Turbulent Inflow Noise Model

The first part of the model derived by Amiet [1, 2] is intended to relate the turbulent inflow, which is idealized as an incoming sinusoidal gust wave, to the pressure difference between upper and lower sides of a flat plate at zero angle of attack. The solution is actually reuniting a theoretical result valid for small spanwise wavenumber of the incoming wave and a second one valid for large wavenumbers. In this section, the solution as formulated by Mish [20] is reported. The second part of the model consists in relating the surface pressure differences across the flat plate to the far field noise. This latter development is not reported herein.

Let first define a few quantities. The chordwise direction is denoted by x, the spanwise direction by y. The half-chord of the flat plate is given as $b = C/2$ where C is the chord. The model will be formulated in a coordinate system non-dimensionalized with b for which the leading edge is located at $x = 0$ and the trailing edge at $x=2$. The wavenumbers in the chordwise and spanwise directions are denoted by k_x and k_y, respectively. The Mach number M is used to define the following parameters:

$$\beta = \sqrt{1 - M^2} \qquad \text{and} \qquad \mu = M k_x/\beta^2$$

The main formula of the theory is the flat plate response function to a sinusoidal gust. It reads:

$$g(x, k_x, k_y) = -\frac{f(x, k_x, k_y)}{\pi\beta}\left\{\pi x\left\{(k_y^2/\beta^2 - \mu^2)^{1/2} + \mathrm{i}(\mu M + k_x)\right\}\right\}^{-1/2} \times \mathrm{e}^{-x(k_y^2/\beta^2-\mu^2)^{1/2}+\mathrm{i}\mu M x}$$

where the function f is given as:

$$f(x, k_x, k_y) = 1 - (x/2)^{1/2}\left\{1 - \mathrm{erf}\left\{\left(2(2-x)(k_y^2/\beta^2 - \mu^2)^{1/2}\right)^{1/2}\right\}\right\}$$

where erf denotes the error function[1].

The pressure difference between the flat plate suction and pressure sides is then given with the coordinate system origin located at mid-span as:

$$\Delta P(x, y, t, k_x, k_y) = 2\pi\rho_0 U_\infty w_0 g(x, k_x, k_y)\mathrm{e}^{\mathrm{i}(k_x U_\infty t - k_y y)}$$

where ρ_0 is the fluid density, U_∞ the inflow velocity (parallel to the x direction), and w_0 the gust amplitude. From this result, the one-sided cross-spectrum of the pressure differences at two points located at chordwise positions x and x' and with spanwise separation length η can be expressed as a function of the frequency f as:

$$S_{\Delta P\Delta P'}(x, x', \eta, f) = 16\,\pi U_\infty(\pi\rho_0 b)^2 \int_0^{+\infty} g^*(x', K_x, k_y)\, g(x, K_x, k_y) \times \Phi_{ww}(K_x, k_y)\mathrm{e}^{\mathrm{i}k_y\eta}\,\mathrm{d}k_y$$

where $K_x = 2\pi f/U_\infty$, and Φ_{ww} is the energy spectrum of the velocity component perpendicular to the flat plate. In the previous formula, the star $(*)$ denotes the complex conjuguate value. In the present model, isotropy is assumed and the derivation by Von Karman yields for the turbulent vertical velocity spectrum:

$$\Phi_{ww}(k_x, k_y) = \frac{4\overline{u^2}}{9\pi k_e^2}\frac{\widehat{k_x}^2 + \widehat{k_y}^2}{(1 + \widehat{k_x}^2 + \widehat{k_y}^2)^{7/3}}$$

[1] Note that the error function is here defined as: $\mathrm{erf}(z) = 2/\sqrt{\pi}\int_0^z \exp(-t^2)\,\mathrm{d}t$ for any complex value z. It is not clear however if the factor $2/\sqrt{\pi}$ is included in the original definition according to Mish [20]

where $\widehat{k_i} = k_i/k_e\,(i = x, y)$, k_e is the wavenumber of the energy-containing eddies, and $\overline{u^2}$ is the turbulent kinetic energy. The wavenumber k_e is well-defined and can be direcly related to the turbulence integral length scale Λ as [15]:

$$k_e = \frac{0.746834}{\Lambda}$$

The turbulent kinetic energy is related to the function of the turbulence intensity I (expressed in %) as:

$$\overline{u^2} = \left(\frac{I}{100}\,U_\infty\right)^2$$

D TNO Trailing Edge Noise Model

This model which was originally proposed by Parchen [22] is gathering several from the previous results. These are used to formulate a far field noise level expression as a function of turbulent boundary layer quantities. These data can be collected from any fluid flow solver which includes a description of the turbulent boundary layer. For example, a panel method coupled to an integral boundary layer formulation as in the software XFOIL [9] can be used. Alternatively, any CFD code including a turbulence model for the boundary layer can be considered.

D.1 Model Formulation

The first part of the model is based on a formula expressing the contribution of the mean-shear/turbulence interaction in the boundary layer and which relates the turbulent boundary layer characteristic data to the fluctuating surface pressure (see Blake [4], Vol.II, p.513, p.524). Using the fact that the wavenumber-frequency spectrum of the wall pressure fluctuations is related to the modulus of its Fourier transform and manipulating, Parchen [22] arrived to the following result for the wavenumber-frequency surface pressure spectrum:

$$\Phi_p(\boldsymbol{k},\omega) = 4\rho_0^2 \frac{k_1^2}{k_1^2+k_3^2} \int_0^{+\infty} L_2(y_2)\,\overline{u_2^2}\left(\frac{\partial U_1}{\partial y_2}(y_2)\right)^2 \Phi_{22}(\boldsymbol{k},\omega) \times \Phi_m(\omega - U_c(y_2)k_1)\,\mathrm{e}^{-2|k|y_2}\,\mathrm{d}y_2 \quad \text{(D.12)}$$

where $|k|$ is the norm of the wavenumber $\boldsymbol{k}=(k_1,0,k_3)$, L_2 is the vertical integral length which characterizes the vertical extent of the turbulent eddies, $\overline{u_2^2}$ is the root mean square (rms) value of the vertical velocity fluctuations, U_1 is the streamwise mean velocity (its derivative, the mean shear, actually appears in the integral), Φ_{22} is the spectrum of the vertical velocity fluctuations (also named the turbulent shear stress), Φ_m is the so-called moving axis spectrum which describes how Φ_{22} is distorted by the generation and destruction of eddies during their convection past the trailing edge, and U_c is the convection velocity of these eddies.

Before relating this wavenumber-frequency spectrum to the far field noise, the two spectra Φ_{22} and Φ_m present in the previous integral across the boundary layer are analytically given using results from turbulence theory.

The moving axis spectrum is assumed to be gaussian and takes the following form:

$$\Phi_m(\omega - U_c k_1) = \frac{1}{\alpha_{\text{Gauss}}\sqrt{\pi}} \mathrm{e}^{-[(\omega - U_c k_1)/\alpha_{\text{Gauss}}]^2}$$

where the gaussian constant α_{Gauss} is a function of the eddy convection velocity and turbulent length scale:

$$\alpha_{\text{Gauss}} = 0.05\,U_c/L_2$$

The convection velocity is in turn a function of the local boundary layer velocity as:

$$U_c(y_2) = c_\alpha U_1(y_2)$$

where the constant c_α is set equal to 0.7.

The Karman three-dimensional kinetic energy spectrum for isotropic turbulence reads:

$$E(k) = \frac{110\,\Gamma(5/6)}{27\sqrt{\pi}\,\Gamma(1/3)} \frac{k_T}{k_e} \frac{(k/k_e)^4}{[1+(k/k_e)^2]^{17/6}} \quad \text{(D.13)}$$

where k_e is the wavenumber of energy containing eddies, and k_T the turbulent kinetic energy. From this equation, the energy density spectrum for the vertical fluctuations in the k_1-k_3 plane can be expressed, assuming again isotropy, as:

$$\Phi_{22}(k_1,k_3) = \frac{4}{9\pi k_e^2}\frac{(k_1/k_e)^2+(k_3/k_e)^2}{[1+(k_1/k_e)^2+(k_3/k_e)^2]^{7/3}} \tag{D.14}$$

The second part of the model consists in expressing the far field noise as a function of the previous wavenumber-frequency spectrum of the surface pressure fluctuations defined by Parchen [22]. Using the results of Chase [8] and Brooks and Hodgson [5], the far field pressure spectrum density can be expressed as an integral of the wall pressure spectrum over the wavenumber component in the flow direction:

$$S(\omega) = \frac{L}{4\pi R^2}\int_{-\infty}^{+\infty}\frac{\omega}{c_0 k_1}\Phi_p(\boldsymbol{k},\omega)|_{k_3=0}\,\mathrm{d}k_1 \tag{D.15}$$

where R denotes the distance of the observer to the trailing edge, and L the span extent of the trailing edge.

At this point, the integral length $\underline{L_2}$, the mean shear $\partial U_1/\partial y_2$, the wavenumber k_e, and the turbulent shear stress $\overline{u_2^2}$ still need to be specified in order to close the model. The specification of these quantities depends on the methodology that is used to calculate the flow field. Two approaches are considered: the integral boundary layer panel code XFOIL [9], and a Reynolds-Average Navier-Stokes solver (in our case EllipSys2D [16, 17, 24]).

D.2 Input from Integral Boundary Layer Method

In the case of a XFOIL calculation, boundary layer equations are solved in order to determine its development along the airfoil chord. This calculation is coupled to a panel method used to compute the inviscid flow outside the boundary layer. The data of interest that are given as an output from XFOIL are: the skin friction coefficient at the wall C_f, the momentum thickness θ, the displacement thickness δ^*, the velocity at the edge of the boundary layer U_0.

The missing data needed for the model proposed in the previous section are obtained using results from classical turbulent boundary layer theory, as well as isotropic turbulence.

The boundary layer thickness δ can be related to the momentum thickness and the displacement thickness by using the relation by Drela and Giles:

$$\delta = \theta\left(3.15+\frac{1.72}{H_k-1}\right)+\delta^*$$

where $H_k=\delta^*/\theta$ is the kinematic shape factor which is also given as an output of XFOIL. The velocity profile can then be approximated in the boundary layer by using Cole's law of the wall/law of the wake [11] as:

$$U_1(y_2) = u^*\left(\frac{1}{\kappa}\ln\left(\frac{u^* y_2}{\nu}\right)+B+\frac{1}{2}W\left(\frac{U_0}{u^*}-\frac{1}{\kappa}\ln\left(\frac{u^*\delta}{\nu}\right)-B\right)\right)$$

where $\kappa=0.41$ is the Karman constant, $B=5.5$, and $u^*=U_0\sqrt{C_f/2}$ is the friction velocity. The wake function is defined as:

$$W = 1-\cos(\pi y_2/\delta)$$

The velocity profile formula can easily be derived to obtain the mean shear.

The next quantity to be defined is the integral length scale L_2. In a first step, the mixing length scale expression proposed by Schlichting [25] is used:

$$l_m = 0.085\,\delta\tanh\left(\frac{\kappa y_2}{0.085\,\delta}\right)$$

Then, the integral length is approximated as:

$$L_2 = \frac{l_m}{\kappa} \tag{D.16}$$

In the case of isotropic turbulence (such an assumption is here needed in order to get the following approximation), the integral length is well defined and related to the wavenumber of the energy-bearing eddies as:

$$L_2 = \frac{\sqrt{\pi}\,\Gamma(5/6)}{\Gamma(1/3)}\frac{1}{k_e} \tag{D.17}$$

yielding:

$$k_e \approx 0.7468/L_2$$

which can be used for evaluating the normal velocity fluctuations spectrum Φ_{22} in Eq.(D.14).

The last quantity to be defined is the turbulent shear stress. Prandtl's mixing length hypothesis assumes that the turbulent viscosity ν_t is related to the mixing length and the mean shear as:

$$\nu_t = l_m^2 \left| \frac{\partial U_1}{\partial y_2} \right|$$

Then, the turbulent kinetic energy k_T is given by:

$$k_T = \sqrt{\nu_t \left(\frac{\partial U_1}{\partial y_2} \right)^2 / C_\mu} \tag{D.18}$$

where $C_\mu = 0.09$. The turbulent shear stress is then assumed proportional to the turbulent kinetic energy as:

$$\overline{u_2^2} = \alpha k_T \tag{D.19}$$

where the constant $\alpha = 0.45$ on the suction side, and $\alpha = 0.3$ on the pressure side of an airfoil.

D.3 Input from RANS Calculation

In the case of a RANS code is used, many of the previous model input data are directly accessible from the computed quantities. In particular, the velocity profile, and thereby the mean shear, accross the boundary layer can be extracted from the velocity field at the trailing edge. Similarly, the turbulent kinetic energy k_T (as well as its dissipation rate ϵ) can be interpolated along the same boundary layer path. Eq.(D.19) is then used to obtain the turbulent shear stress $\overline{u_2^2}$.

The integral length scale is the last remaining quantity to be defined. Wagner *et al* [27] used the simple assumption that the vertical correlation length is proportional to the mixing length scale as in Eq.(D.16).

Lutz *et al* [14] argues that the determination of the vertical length scale is most crucial for the consistency of the noise prediction. Therefore, a more elaborate approach to evaluate L_2 is proposed. In the case of isotropic turbulence, the integral length is well defined as a function of the wavenumber of the energy-bearing eddies as:

$$L_2 = \frac{\sqrt{\pi}\,\Gamma(5/6)}{\Gamma(1/3)}\frac{1}{k_e}$$

The Kolmogorov spectrum in the inertial subrange reads:

$$E(k) = C\frac{\epsilon^{2/3}}{k_T^{5/3}}$$

where the constant $C \approx 1.5$ was experimentally determined, and ϵ is the turbulent energy dissipation rate. By comparing the previous spectrum with the asymptotic behavior of the Karman spectrum in Eq.(D.13), the wavenumber of the energy bearing eddies k_e can be deduced:

$$k_e \approx 1.9275 \frac{\epsilon}{k_T^{3/2}}$$

Combining this equation with the above equation relating the wavenumber k_e and the integral length L_2 in the case of isotropic turbulence, the following result can be established:

$$L_2 \approx 0.387 \frac{k_T^{3/2}}{\epsilon} \tag{D.20}$$

This latter approach will be used in the following noise calculations based on RANS computational results (instead of using Eq.(D.16)).

Note that in the original model proposed by Parchen [22], an alternative approximation for the vertical integral length scale that can be employed in conjunction with a Reynolds-Averaged Navier-Stokes solution method was proposed. The mixing length is first approximated by:

$$l_m = \frac{C_\mu^{3/4} k_T^{3/2}}{\epsilon}$$

Then, combining with Eq.(D.16) relating the mixing length scale to the integral length scale, this yields:

$$L_2 \approx 0.401 \frac{k_T^{3/2}}{\epsilon}$$

which is very similar to Eq.(D.20).